Tectonophysics 766 (2019) 94–114

Contents lists available at ScienceDirect

Tectonophysics

journal homepage: www.elsevier.com/locate/tecto

Strain rate and stress fields in the West and South Lut block, Iran: Insights from the inversion of focal mechanism and geodetic data

Ahmad Rashidi[a,*], Mohamad Mahdi Khatib[b], Faramarz Nilfouroushan[c,d], Reza Derakhshani[e,f], Seyed Morteza Mousavi[b], Hossein Kianimehr[a,g], Yahya Djamour[h]

[a] International Institute of Earthquake Engineering and Seismology, Tehran, Iran
[b] Department of Geology, University of Birjand, Birjand, Iran
[c] Department of Industrial Development, IT and Land Management, University of Gävle, Gävle, Sweden
[d] Lantmäteriet, Gävle, Sweden
[e] Department of Geology, Shahid Bahonar University of Kerman, Kerman, Iran
[f] Department of Earth Sciences, Utrecht University, 3584 CB Utrecht, the Netherlands
[g] Iranian Seismological Center, Institute of Geophysics, University of Tehran, Tehran, Iran
[h] Geomatics College, National Cartographic Center of I.R., Tehran, Iran

ARTICLE INFO

Keywords:
Tectonic regime
Stress inversion
Strain rate
Moment rate
Lut block
Iran

ABSTRACT

The active tectonic deformation and hazardous earthquakes in the south and west of the Lut block have been investigated for a long time. In this study, we compute the geodetic and seismic strain rates using focal mechanism data from the Harvard CMT catalogue and various other sources including the published GPS velocities. Moreover, we also perform Focal Mechanism Stress Inversion (FMSI) to deduce a stress model for the region. Our study shows an expected correlation between the stress orientations, seismic and geodetic strain rates. Our results show that the south and west of the Lut block is generally exposed as a compressional strike-slip tectonic regime. The tectonic convergence in this area is taken up not only by motions along and across the faults but also by the rotation of those blocks which bounded by these faults. The maximum amount of rotation rate is observed where there are the main right lateral strike slip fault systems such as Sabzevaran, Gowk, Nayband, Bam, Kuhbanan, and Kahurak. The orientation of the mean stress direction, obtained from the FMSI results in the west and south of the Lut block, is approximated ~N19 E. In this area, faults are almost oblique relative to the tectonic motion direction. Moreover, there are right-lateral and left-lateral shears, in addition to the dip movements in different parts of the south and west of the Lut block. Our analyses show three main categories of the stress regimes including strike-slip faulting (43.2%), thrust faulting (38.6%), and unknown or oblique faulting (18.2%).

We also calculated seismic and geodetic moment rates for this area, which indicate the seismic moment rate is relatively high between Bam and Shahdad where there are some segments of the Gowk fault.

1. Introduction

Many studies have been conducted to investigate the active tectonics of Iran, located in a convergence zone between Arabian and Eurasian plates. The convergence in this region is mostly accommodated by the Zagros Mountains in the west and the southwest, Alborz and Kopeh-Dagh in the north and the northeast of Iran, Makran in the southeast of Iran, and the N−S strike-slip faulting in eastern Iran (Fig. 1, DeMets et al., 1994; Jackson, 1992; Mehrabi et al., 2015). The tectonics of Iran is especially characterized by active faulting, Quaternary volcanism and large destructive earthquakes. During the 1900–2018 period, at least 190,290 human fatalities resulted from 139 earthquakes in Iran in which 11 of them were larger than magnitude 7 (National Geophysical Data Center, NOAA, 2016). A substantial part of the earthquake fatalities is due to tectonic activities along the eastern and western margins of the Lut block, which is considered as a rigid block with a thin crustal structure (Dehghani and Makris, 1984). The eastern limit of the Lut block is Nehbandan fault system. The Nehbandan fault overprints the Sistan suture zone, which represents an accretionary prism that was emplaced during of the N-S-trending Sistan ocean which

* Corresponding author at: International Institute of Earthquake Engineering and Seismology, No. 21, Arghavan St., North Dibajee, Farmanieh, Tehran, P.O. Box 19537-14453, Iran.
E-mail address: rashidi@iiees.ac.ir (A. Rashidi).

https://doi.org/10.1016/j.tecto.2019.05.020
Received 27 May 2018; Received in revised form 21 May 2019; Accepted 27 May 2019
Available online 11 June 2019
0040-1951/ Published by Elsevier B.V.

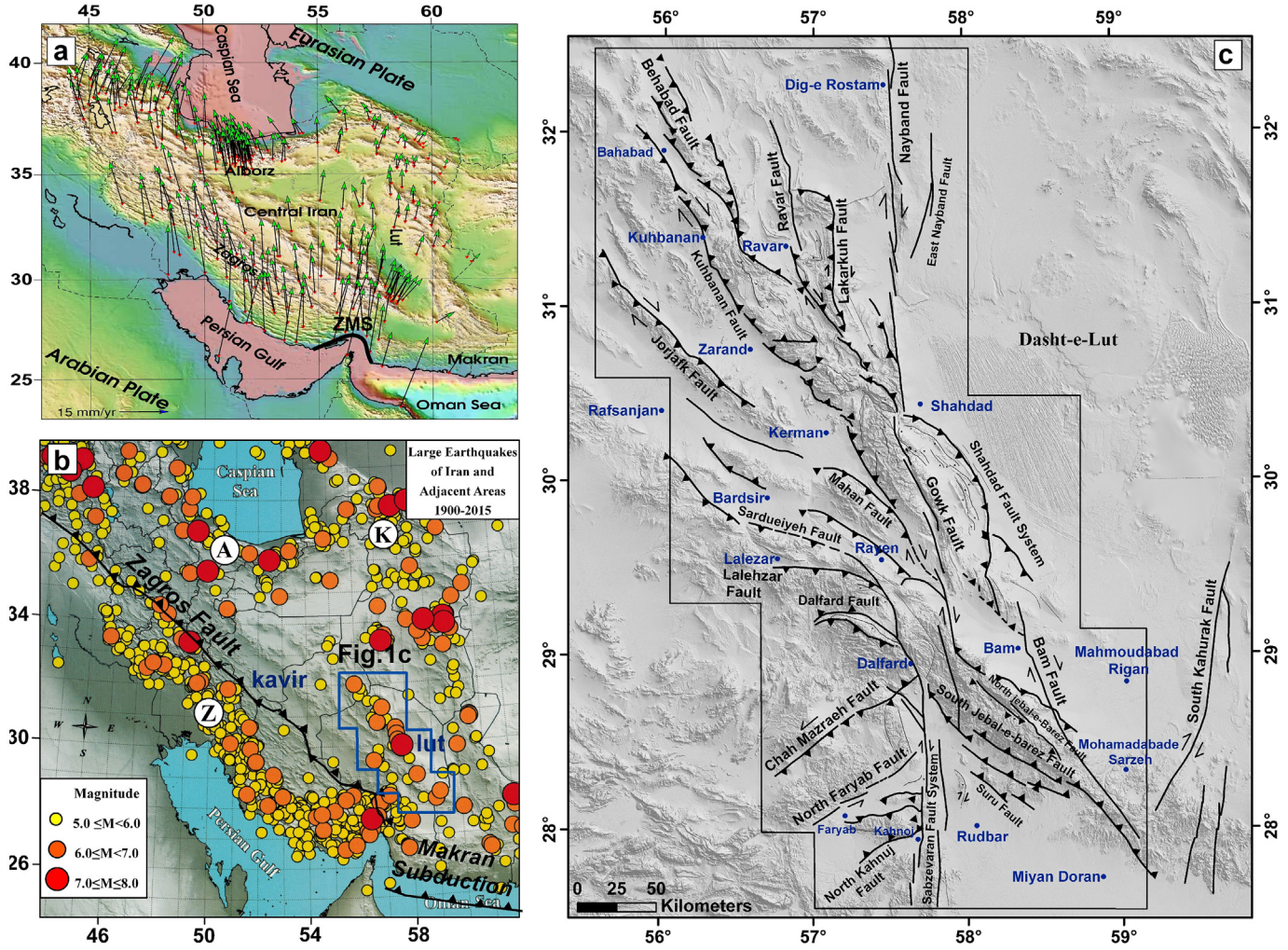

Fig. 1. (a) The GPS velocity field relative to Eurasia in Iran (Zarifi et al. (2014) and Walpersdorf et al. (2014)). ZMS: Zagros Makran Syntaxis. (b) The filled circles show 5+ earthquakes taken from the ISC Catalogue (2015). Z, A, and K stand for Zagros, Alborz, and Kopeh Dagh, respectively. (c) Shaded-relief topographic map of the west and south of the Lut region with active faults.
(After Rashidi et al., 2017)

once separated the Lut and Afghan block (Şengör et al., 1988). The western limit of the Lut block is separated from central Iran through a number of N-S to NNW-SSE striking right-lateral fault systems, including the Nayband, Gowk and Sabzevaran (Fig. 1c, Rashidi et al., 2017).

The study area is located in the W-S Lut block as shown in Fig. 1. Ten destructive earthquakes, from 1977 to 2012, were accompanied by about 185 km of the surface rupture in the South and Southwest of the Lut block. These earthquakes have resulted in ~44,700 human fatalities, ~36,646 injured and more than 100,000 homeless. There is no reliable estimation of the seismic-interseismic evolution of the active faults in this region; therefore, the seismic hazard assessment is not accurate enough. It is important that the seismicity of the area and its temporal and spatial variations are viewed as snapshots of the ongoing tectonic activities. Therefore, identification of the interseismic and seismic strain rate with interseismic moment rate patterns may provide complementary deductions for more realistic analysis and interpretation of the observations.

The local and regional stress fields in Iran were discussed and estimated in various studies using the stress inversion of earthquake focal mechanism in the Zagros (Gillard and Wyss, 1995; Lacombe et al., 2006; Navabpour et al., 2007, 2008), the Alborz (Zanchi et al., 2006) and the Kopeh Dagh (Zamani et al., 2008). Furthermore, numerical investigation of seismic deformation (Derakhshani and Eslami, 2011) and comparison of the seismic and aseismic deformation in Iran using GPS velocities and earthquake data have been carried out (Masson et al., 2005; Raeesi et al., 2017; Zarifi et al., 2014). In this study, we included more GPS stations data (Fig. 1a) than previous studies (Masson et al., 2005; Zarifi et al., 2014) and divided our study area to more detailed triangular grids to investigate the distribution and localization of strain and moment rates.

The purpose of the present study is using all available earthquake focal mechanisms and geodetic data to establish a present-day stress map for the West and South of the Lut block (Fig. 1). We investigate the role of the seismic and the geodetic strain and moment rates in the seismicity of the study area. Moreover, based on our field observations and the results of seismic data analysis, we highlight the dominant tectonic regimes in this area.

2. Tectonic setting and seismicity

The active tectonics of the Iranian plateau is the consequence of the convergence between the Arabian and Eurasian plates (Fig. 1a) in which the deformation and seismicity of southern Iran are mainly affected by the northeastward motion of the Arabian plate (Fig. 1b). The GPS studies indicate that the deformation distribution in Iran is heterogeneous and different faults or blocks accommodate a part of this convergence deformation (Nilforoushan et al., 2003; Vernant et al.,

2004; Khorrami et al., 2019).

The Late Pleistocene and Holocene right-lateral slip rates along the western margin of the Lut block, at longitude ~57°45′E, increase from the north to the south. This southward increased activity, which indicates the complexity of the structural evolution, is inferred from the slip rates of Nayband, 1.8 ± 0.7 mm/yr (Foroutan et al., 2014); Gowk, 3.8 ± 0.7 mm/yr (Walker et al., 2010) and Sabzevaran fault, 5.7 ± 1.7 mm/yr (Regard et al., 2006). The Sabzevaran fault is located in the transitional zone between Zagros and Makran stress fields, the Zagros continental collision zone (in the west) and Makran subduction zone (in the east). Along the Gowk and Nayband faults, deformations are related to the different slip rates of the NS faults (Nayband and Gowk faults) and to the different slip rates in the EW direction (Gowk and Nayband faults with Anar fault). Therefore, the west boundary of the Lut block, and also southward to the southeast of Urumieh-Dokhtar Cenozoic magmatic zone by these shear systems, has experienced intense and young deformation in different parts of this area (Amirihanza et al., 2018; Mirzaie et al., 2015). As such, different slip rates have caused a different level of seismicity in different parts of the area. Some studies have suggested a few numbers of new faults in the South and West of the Lut block (Rashidi Boshrabadi et al., 2018) in which we have used in this study. We analyze the relationships between strain rates, rotation rates and their directions with the mechanism of the old and new faults.

There is a complete absence of historical records of earthquakes until ~160 years ago, but a substantial number of earthquakes, mainly instrumental, are reported for the study area. The lack of historical records may be resulted from isolation of the area due to proximity to deserts (Ambraseys and Melville, 2005; Berberian, 2005). The destructive earthquakes with the gaps in the south, along the Sabzevaran fault and also in the north, along the Nayband fault, are noticeable. However, a large number of small earthquakes are recorded along with these segments. In addition, the young sediments along with the mentioned segments have cut by these faults. These indications may infer the potential for the occurrence of the destructive earthquakes along with these segments in future.

3. Seismic strain and stress fields

In order to elaborate on the tectonic deformation, the comparison of the seismic and geodetic deformation can play a significant role in earthquake hazard assessment. This comparison marks the zones with higher seismic deformation and can be correlated with the large earthquake distributions. Furthermore, we can discuss our results in term of the crustal deformation processes.

Because of the large distance between some of the GPS sites on either side of the faults, we assume that the co- and post-seismic local deformation at the location of benchmarks are negligible all along the seismic cycle and as such the geodetic strain rates represent the interseismic strain rates.

To this end, the seismic events with reliable source parameters were selected from various sources (Fig. 2 and Table 1) in order to compute the seismic strain-rate tensor using the Kostrov's formulation (Kostrov, 1974) and Win-Tensor program (Delvaux and Sperner, 2003). In addition, in order to compare the results of seismic and geodetic strain-rate in different parts of the study area, the triangular networks were used for computations where there are at least 3 events with the reliable focal mechanism. Some earthquakes were used in two networks due to their location in the boundary between two triangle networks. However, no event source parameters were available in triangles 1 and 2 because of the lack of significant historical or instrumental earthquake mechanisms (Fig. 2).

3.1. Stress orientations

The stress inversion was carried out to obtain the direction of the principal stress axes. Generally, the stress analysis is based on this fact that the direction of maximum shear stress is within the dislocation plane (Bott, 1959). The stress tensor including the orientation of the three orthogonal principal stress axes (σ1, σ2, σ3) and the stress ratio, R, are determined from fault plane and slip parameters (Eq. (1)).

$$R = \frac{\sigma_2 - \sigma_3}{\sigma_1 - \sigma_3} \quad (1)$$

In this study, two different stress inversion methods, Right Dihedrom (Angelier and Mechler, 1977) and Rotational optimization (Delvaux and Sperner, 2003), were used to obtain stress tensor. The focal mechanisms of earthquakes are generally used to analyze stress fields. Basically, it is assumed that all of the mechanisms are affected by the same stress regime according to the focal mechanism inversion methods. The Right Diherdron method is implemented to determine the principal stress axes (T, B, and P) (Angelier and Mechler, 1977). The results of an equal-area projection indicate the limitation of this method to distinguish the stress axis. Thus, in order to overcome the limitation, the results of the Diherdron method are also used as a priori estimation for the Rotational Optimization method.

The Rotational Optimization introduced by Delvaux and Sperner (Delvaux and Sperner, 2003) is a method in the focal mechanism data inversion. Removing the improper tensor elements in minimizing the errors is regarded as one of the advantages of this method. The stress inversion of the focal mechanisms is based on two assumptions: 1) the stress field is homogeneous and constant in the space and time, 2) the occurrence of earthquake slip is in the direction of the maximum shear stress.

3.2. Tectonic stress parameter (R′)

In order to express the numerical value of the tectonic stress regime in the area, the stress regime parameter (R′) was used based on the obtained stress ratio (Eq. (1)). The types of stress regime have been studied by Delvaux et al. (1997) and Delvaux and Sperner (2003) and are characterized as follows:

for normal faulting regimes $R' = R$ (2)

for strike − slip faulting regimes $R' = (2 - R)$ (3)

for thrust faulting regimes $R' = (2 + R)$ (4)

The tectonic regime is normal when the obtained R' is in the range of 0–1 while the values in the ranges of 1–2, and 2–3 are for strike-slip and thrust faulting regimes, respectively.

3.3. Results of stress analysis using focal mechanisms

The moment stress axes P, T, and B (Table 2) represent the maximum shortening, the maximum extension, and the unbiased axis, respectively. In addition, the focal mechanism solution was used based on the Right Dihedrom method developed in the Win-Tensor software (Delvaux and Sperner, 2003).

The direction of the horizontal stress is usually demonstrated according to two perpendicular horizontal axes including Sh_{max} as the maximum horizontal axis and Sh_{min} as the minimum horizontal stress one. The Zoback and Lund-Townend methods are used to calculate the horizontal axes (Lund and Townend, 2007; Zoback, 1992a), among which the Lund-Townend method is utilized in the Win-Tensor program (Table 2 and Fig. 4).

The stress regimes were obtained based on the WSM (World Stress Map) standard. The strike-slip faulting, thrust faulting with a strike-slip component, thrust faulting, normal faulting, normal faulting with a strike-slip component, as well as the unknown or oblique regimes are symbolized by SS, TS, TF, NF, NS, and UF, respectively. These tectonic regimes are obtained for each earthquake according to the Zoback method (Zoback, 1992b) developed in the Win-Tensor program

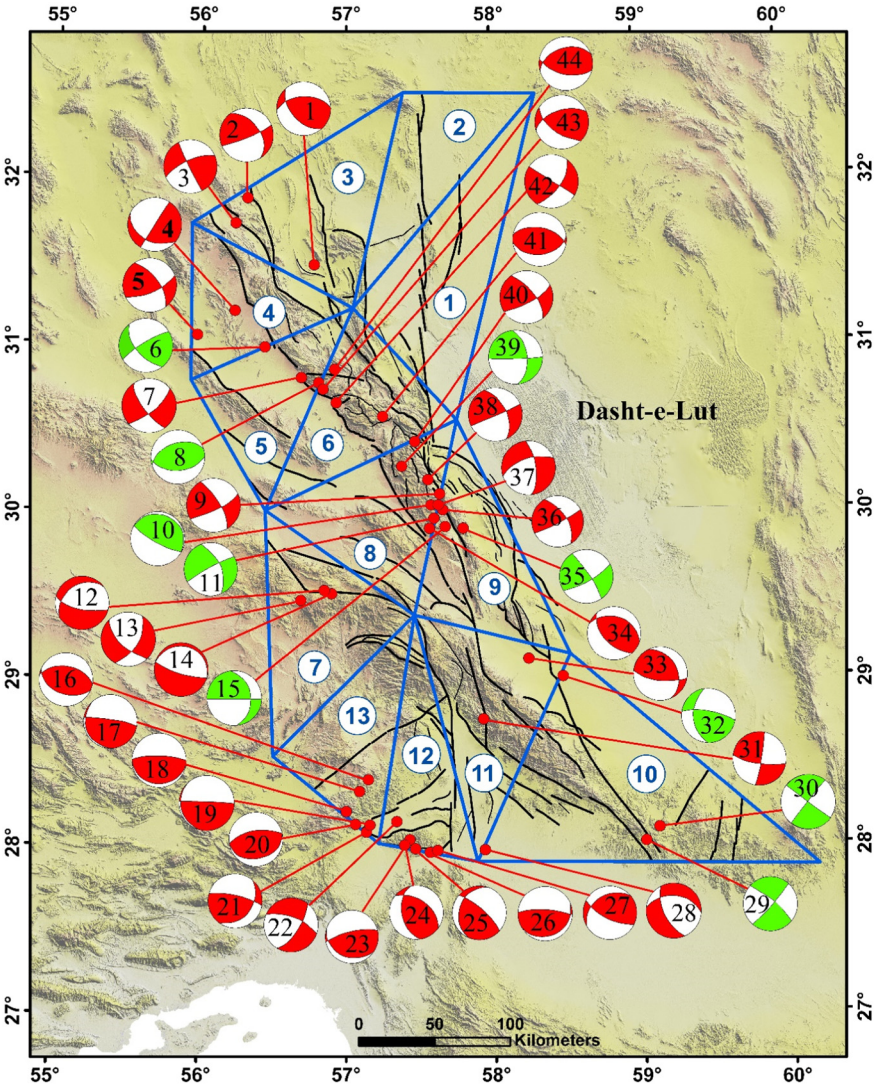

Fig. 2. The used focal mechanisms data in the study area from 1964 to 2015 from various catalogues (After Rashidi Boshrabadi et al., 2018). The green color focal mechanisms are related to the destructive earthquakes with surface ruptures in the period of 1977 to 2012. (For interpretation of the references to color in this figure legend, the reader is referred to the web version of this article.)

(Table 2).

The statistical evaluation of the stress regimes in the study area indicates that 43.19%, 38.63%, and 18.18% of the tectonic regimes are related to strike-slip, thrust, and unknown faultings, respectively (Fig. 3). This is consistent with previous studies on active tectonics in the west and south of the Lut block which reported the high activity of the strike slip and the reveres faults in this part of Iran.

3.4. Stress inversion

Stress inversion is necessary to determine the principal stress values (σ_1, σ_2, σ_3) obtained using the focal mechanisms (Delvaux and Sperner, 2003). Based on the distribution of the GPS velocities and the fault locations, we divided the area into 13 triangular networks. The stress inversion was carried out using the Dihedron and Rotational Optimization methods for the earthquakes within each network (Fig. 4).

According to the stress inversion results (Fig. 4), no significant difference is observed in two used methods However, the obtained results are likely more accurate due to adjusting errors in the Rotational Optimization method (Table 3). SH_{max} and Sh_{min} are regarded as the azimuth of maximum and minimum axes of seismic strain rate, respectively (Fig. 5).

3.5. Seismic strain rate

In this study, the seismic strain rate was calculated using the Kostrov formula (Eq. (5), Kostrov, 1974). According to Kostrov (1974), V as the seismic strain tensor in an area depends on the total seismic moment tensor within that area if the strain takes place in a seismic volume.

$$\dot{\varepsilon} = \frac{1}{2\mu Vt}\sum_{n=1}^{N} M_{ij}^{n} = \frac{1}{2\mu Vt}M_{ij} \quad (5)$$

where μ represents the shear modulus, V is deforming seismic volume, N is the total number of events in the time period of t, M_{ij}^{n} shows the seismic moment tensor element for the events, and Mij is regarded as the total seismic tensors. It is worth noting that μ, V, and play a significant role only on the strain and not on the directions of the principal strain axes (Bus et al., 2009). In order to estimate the volume of the study area, the thickness of seismogenic zone was considered to be 15 km based on the previous studies (Jackson and McKenzie, 1988; Means, 2012; Zarifi et al., 2014). The Aki and Richard's approach (Eq. (6); Aid and Richards, 1980) were used to calculating the seismic strain tensor elements based on the inversion of focal mechanisms within the study area (Eq. (6)):

Table 1
The earthquake source parameters used to obtain the seismic strain-rate shown in Fig. 2. The φ, δ and λ symbols represent the strike, dip and rake angles of the preferred nodal planes. The labels in the last column refer to the focal mechanisms shown in Fig. 2. Italic rows are destructive earthquakes with a surface rupture from 1977 through 2012.

Date	Time	Lat.	Lon.	Mag	Dep.	φ	δ	λ	Mo	Ref.	Label
2012/02/27	18:48:55	31.464	56.778	5.1	6	317	52	126	6.32E+23	IRSC	1
2015/10/29	15:48:18	32	56.15	4.2	11	148	50	167	2.69E+22	IRSC	2
2002/04/05	18:40:19	31.85	56.07	5.2	33	334	86	162	6.70E+23	CMT	3
2002/10/16	09:20:45	31.19	56.23	5.3	33	31	88	53	9.59E+23	CMT	4
1978/05/22	06:18:12	31.25	55.73	5.1	15	144	65	155	5.23E+23	IRIS	5
1977/12/19	*23:34:34*	*30.95*	*56.47*	*5.8*	*31*	*322*	*60*	*168*		*M97*	*6*
2006/05/07	06:20:57	30.79	56.69	5	12	228	73	−19	3.41E+23	CMT	7
2005/02/22	*02:25:30*	*30.76*	*56.81*	*6.4*	*12*	*71*	*44*	*79*	*5.20E+25*	*CMT*	*8*
2015/07/31	10:06:29	30.096	57.64	5.3	15	148	72	164	1.07E+24	IRSC	9
1981/07/28	*17:22:43*	*30.03*	*57.58*	*7.2*	*15.2*	*300*	*79*	*84*	*9.01E+26*	*CMT*	*10*
1998/03/14	*19:40:34*	*29.95*	*57.6*	*6.6*	*15*	*154*	*57*	*−174*	*9.43E+25*	*CMT*	*11*
1970/11/09	17:41:42	29.52	56.85	5.4	6	284	71	−66		M97	12
2010/07/31	06:52:58	29.46	56.69	5.4	18.1	314	68	−147	1.66E+24	CMT	13
1970/11/08	17:42	29:5	56:9	5.4	6	287	80	−90		M97	14
1981/06/11	*07:24:34*	*29.69*	*57.36*	*6.7*	*20*	*172*	*37*	*171*		*M97*	*15*
1993/04/12	14:00:52	28.39	57.15	4.9	33	103	46	84	3.32E+23	CMT	16
1996/02/26	08:08:23	28.32	57.09	5.5	33	100	84	86	2.35E+24	CMT	17
1964/12/22	04:36:35	28.2	57	5.4	42	92	76	90		M97	18
2011/03/05	20:42:52	28.12	57.16	5.2	15.7	93	87	86	6.75E+23	CMT	19
2015/03/05	22:54:50	28.078	56.97	4.7	19	81	64	94	1.52E+23	IRSC	20
1991/12/19	18:55:21	27.97	57.06	5.4	15	103	75	123	1.42E+24	CMT	21
2004/10/07	12:54:59	28.14	57.34	5	12	211	67	−156	3.67E+23	CMT	22
1997/10/20	06:09:09	27.98	57.45	5.4	33	77	72	78	1.54E+24	CMT	23
2014/06/02	22:51:17	27.874	57.390	4.6	32	127	53	62	1.09E+23	IRSC	24
2014/10/24	12:38:56	27.8	57.42	4.8	26	132	76	68		IRSC	25
1999/03/04	05:38:34	27.91	57.49	6.6	26	93	75	96	1.01E+26	CMT	26
2014/05/09	00:08:45	27.921	57.540	4.7	40	52	32	29	1.65E+23	IRSC	27
2012/04/18	17:40:42	27.867	58.077	5	65	334	61	−53	4.21E+23	IRSC	28
2011/01/27	*08:38:31*	*28.02*	*59.02*	*6.2*	*14.3*	*129*	*77*	*−5*	*2.42E+25*	*CMT*	*29*
2010/12/20	*18:42:06*	*28.1*	*59.11*	*6.5*	*14.8*	*126*	*90*	*3*	*8.26E+25*	*CMT*	*30*
2004/10/06	11:14:31	28.75	57.93	5.2	48.5	189	86	165	7.62E+23	CMT	31
2003/12/26	*01:56:00*	*28.95*	*58.26*	*6.6*	*6*	*354*	*86*	*−182*	*7.60E+18*	*CMT*	*32*
2004/07/22	04:51:39	29.11	58.24	4.7	17.2	152	38	138	1.53E+23	CMT	33
2011/06/26	19:46:56	29.89	57.57	5.1	21.5	114	36	71	6.10E+23	CMT	34
1989/11/20	*04:19:11*	*29.89*	*57.8*	*5.9*	*15*	*148*	*81*	*165*	*8.18E+24*	*CMT*	*35*
2015/02/17	13:41:36	30	57.66	4.6	4	148	61	173	8.63E+22	IRSC	36
2015/07/25	16:10:41	30.03	57.63	4.6	18	172	68	−150	9.80E+22	IRSC	37
2015/02/13	01:00:44	30.18	57.56	4.1	8	155	57	178	1.96E+22	IRSC	38
1998/11/18	*07:39:22*	*30.26*	*57.38*	*5.3*	*15*	*174*	*55*	*173*	*1.29E+24*	*CMT*	*39*
2013/01/21	19:48:58	30.407	57.471	5.3	5	142	66	160	1.01E+24	IRSC	40
2012/12/03	12:53:22	30.558	57.25	4.7	11	101	53	101	1.22E+23	IRSC	41
2005/05/01	18:58:41	30.64	56.93	5.1	20.3	122	87	153	5.84E+23	CMT	42
2005/05/14	18:04:58	30.72	56.84	5.2	12	69	53	46	9.00E+23	CMT	43
1984/08/06	11:14:39	30.84	56.92	5.4	18.7	72	39	66	1.50E+24	CMT	44

$$F_{XX} = -(sin\delta cos\theta sin2\varphi + sin\,2\delta sin\theta sin2\varphi)$$

$$F_{XY} = sin\delta cos\theta cos2\varphi + 0.5\,sin\,2\delta sin\theta sin2\varphi$$

$$F_{XZ} = -(cos\delta cos\theta cos\varphi + cos\,2\delta sin\theta sin\varphi)$$

$$F_{YY} = sin\delta cos\theta sin2\varphi - sin\,2\delta sin\theta cos2\varphi$$

$$F_{YZ} = -(cos\delta cos\theta sin\varphi - cos\,2\delta sin\theta cos\varphi)$$

$$F_{ZZ} = sin\,2\delta sin\theta$$

$$F_{XY} = F_{YX}$$

$$F_{XZ} = F_{ZX}$$

$$F_{YZ} = F_{ZY}$$

(6)

where φ is the fault azimuth, δ is dip and θ is the rake parameter. According to the direction and relative magnitude of principal axes of seismic strain rate in each triangle (Table 4; Fig. 5) in the south of the study area, the seismic strain rate is dominant. In this area, main earthquakes such as the Rigan earthquake (2010/12/20, 2011/01/27), the Bam earthquake (2003/12/26) and the Kahnouj earthquake (1997/12/20, 1999/03/04) occurred by the activity of Kahourak, Bam and segments of Sabzevaran faults.

4. Geodetic strain field

The interseismic strain rates and the directions of strain axes are calculated from the GPS velocities. These parameters can explain the dynamics of the crust and the strain accumulation around the fault traces. The study of strain accumulation plays a crucial role in the seismic hazard assessment, and analysis of strain tensor can evaluate different aspects of the surface deformation.

4.1. Geodetic strain rate

In this study, the Delaunay triangulation method and GPS velocities were used to calculate the geodetic strain rate, and the geodetic strain rate was obtained from velocity gradient tensor in each triangle. The velocity gradient tensor is the combination of differential deformation and the rotation components. Each tensor is decomposed to a symmetric and an asymmetric part which represents the strain and the rotation rate, respectively (Malvern, 1969).

To compare the geodetic and seismic strain rates, we used the triangular geometry (Fig. 4) in both the seismic and geodetic data analysis.

In order to estimate the kinematic of the study area, the GPS

Table 2
Obtained parameters from the stress tensor using the focal mechanisms in the study area.

No.	Date (y.m.d)	Fault plane		Slip line		Slip	Moment stress axes						SH		R′	Reg.
		Dip	Dip dir.	Plunge	Azim.	Sense	P		B		T		Max	Min		
							Incl.	Azim.	Incl.	Azim.	Incl.	Azim.				
1	2012.02.27	52	227	40	177	ID	1	202	28	293	62	110	22	112	2.5	*TF*
2	2015.10.29	50	238	10	156	ID	19	11	48	257	35	115	17	107	1.5	*SS*
3	2002.04.05	86	244	18	155	ID	10	201	72	322	15	108	20	110	1.5	*SS*
4	2002.10.16	88	301	53	28	IS	33	331	37	213	36	89	164	74	1.5	*UF*
5	1978.05.22	65	54	23	335	ID	1	194	55	102	35	285	14	104	1.5	*SS*
6	*1977.12.19*	*60*	*232*	*10*	*148*	*ID*	*13*	*7*	*58*	*254*	*28*	*104*	*10*	*100*	*1.5*	*SS*
7	2006.05.07	73	138	18	54	NS	25	6	65	188	1	96	6	96	1.5	*SS*
8	*2005.02.22*	*44*	*341*	*43*	*356*	*IS*	*2*	*169*	*8*	*259*	*82*	*68*	*169*	*79*	*2.5*	*TF*
9	2015.07.31	72	58	15	333	ID	2	195	66	100	24	286	15	105	1.5	*SS*
10	*1981.07.28*	*79*	*210*	*77*	*239*	*IS*	*34*	*215*	*6*	*121*	*56*	*22*	*45*	*135*	*2.5*	*TF*
11	*1998.03.14*	*57*	*64*	*5*	*151*	*ND*	*27*	*192*	*57*	*53*	*19*	*292*	*17*	*107*	*1.5*	*SS*
12	1970.11.09	71	194	60	248	IS	22	212	22	112	57	342	41	131	2.5	*TF*
13	2010.07.31	68	224	30	148	ID	5	188	51	284	38	93	6	96	1.5	*SS*
14	1970.11.08	80	17	80	17	IX	35	17	0	107	55	197	17	107	2.5	*UF*
15	*1981.06.11*	*37*	*82*	*5*	*359*	*ID*	*30*	*208*	*37*	*93*	*39*	*326*	*40*	*130*	*2.5*	*UF*
16	1993.04.12	46	13	46	22	IS	1	17	4	287	85	120	17	107	2.5	*TF*
17	1996.02.26	84	10	83	44	IS	39	14	4	280	51	186	27	117	2.5	*UF*
18	1964.12.22	76	2	76	2	IX	31	2	0	92	59	182	2	92	2.5	*TF*
19	2011.03.05	87	3	85	56	IS	42	7	4	273	48	179	30	120	2.5	*UF*
20	2015.03.05	64	351	64	342	ID	19	348	4	79	71	179	166	76	2.5	*TF*
21	1991.12.19	75	13	54	305	ID	23	348	32	93	49	229	159	69	2.5	*UF*
22	2004.10.07	67	121	22	201	ND	33	251	57	72	1	341	71	161	1.5	*SS*
23	1997.10.20	72	347	68	22	IS	26	357	12	261	61	149	5	95	2.5	*TF*
24	2014.06.02	53	37	45	78	IS	4	56	22	324	68	157	57	147	2.5	*TF*
25	2014.10.24	76	42	64	101	IS	28	59	21	318	54	195	71	161	2.5	*TF*
26	1999.03.04	75	3	74	341	ID	30	358	6	91	60	191	172	82	2.5	*TF*
27	2014.05.09	32	322	15	27	IS	25	185	28	289	51	60	174	84	2.5	*UF*
28	2012.04.18	61	244	44	301	IS	9	269	32	174	57	13	92	2	2.5	*TF*
29	*2011.01.27*	*77*	*36*	*5*	*307*	*NS*	*13*	*262*	*76*	*58*	*6*	*171*	*81*	*171*	*1.5*	*SS*
30	*2010.12.20*	*90*	*36*	*3*	*126*	*IS*	*2*	*81*	*87*	*306*	*2*	*171*	*81*	*171*	*1.5*	*SS*
31	2004.10.06	86	99	15	10	ID	8	55	74	174	13	324	54	144	1.5	*SS*
32	*2013.12.26*	*86*	*264*	*2*	*174*	*ID*	*1*	*39*	*86*	*291*	*4*	*129*	*39*	*129*	*1.5*	*SS*
33	2004.07.22	38	62	24	7	ID	16	209	27	110	58	325	35	125	2.5	*TF*
34	2011.06.26	36	24	34	47	IS	10	217	11	309	75	86	35	125	2.5	*TF*
35	*1989.11.20*	*81*	*58*	*15*	*330*	*ID*	*4*	*15*	*72*	*118*	*17*	*283*	*14*	*104*	*1.5*	*SS*
36	2015.02.17	61	58	6	331	ID	16	191	60	72	25	288	15	105	1.5	*SS*
37	2015.07.25	68	82	28	160	ND	37	213	53	25	4	120	31	121	1.5	*SS*
38	2015.02.13	57	65	2	336	ID	21	196	57	69	24	296	21	111	1.5	*UF*
39	*1998.11.18*	*55*	*84*	*6*	*358*	*ID*	*19*	*216*	*54*	*96*	*29*	*317*	*41*	*131*	*1.5*	*SS*
40	2013.01.21	66	52	18	330	ID	4	190	59	93	30	282	11	101	1.5	*SS*
41	2012.12.03	53	11	52	353	ID	8	3	9	94	78	233	2	92	2.5	*TF*
42	2005.05.01	87	32	27	304	ID	17	351	63	116	21	255	168	78	1.5	*SS*
43	2005.05.14	53	339	35	37	IS	1	188	34	279	56	97	8	98	2.5	*TF*
44	1984.08.06	39	342	35	12	IS	8	179	15	271	73	61	177	87	2.5	*TF*

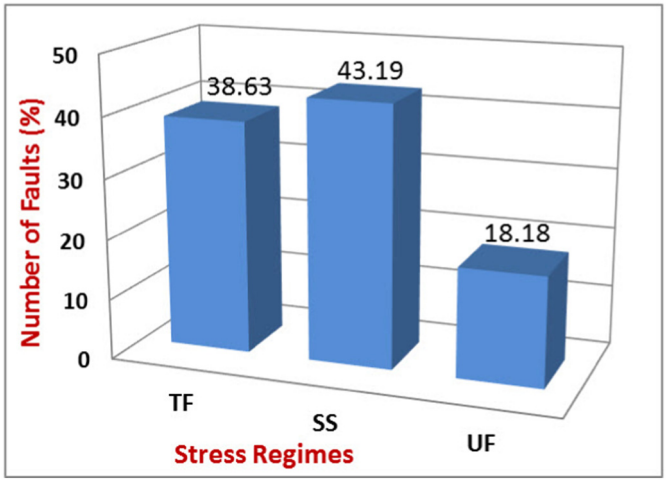

Fig. 3. The statistical assessment of the stress regimes obtained from focal mechanisms in the study area. SS, TF, UF symbols are Strike-Slip, Thrust and Unknown (or oblique) Faulting respectively.

velocities reported in Walpersdorf et al. (Walpersdorf et al., 2014) were used. The GPS velocity field is relative to the Eurasian reference frame (Table 5). The velocity vectors clearly demonstrate a straight edge in the west and south of the Lut block.

The geodetic strain rate was calculated for each Delaunay triangle by using the GPS velocities (Table 6; Fig. 6).

As displayed in Fig. 6, there is a dominant compression axis with a NE-SW trend which has an oblique orientation relative to the fault trends in most of the triangles. In addition, the extension in most of the triangles indicates the strike-slip kinematics in the study area. In some triangles such as 8 and 9, the amount of horizontal extension rate is maximum where the main faults are the Gowk, Rayen and Mahan (Fig. 1c) in which the slip rate accumulation occurs (Rashidi Boshrabadi et al., 2018). Moreover, in triangles 11 and 12 near to the transitional zone between the Zagros, Central Iran and Makran, the horizontal extension rate has high values.

4.2. Geodetic rotation rate

The displacement gradient tensor is the sum of a symmetric tensor

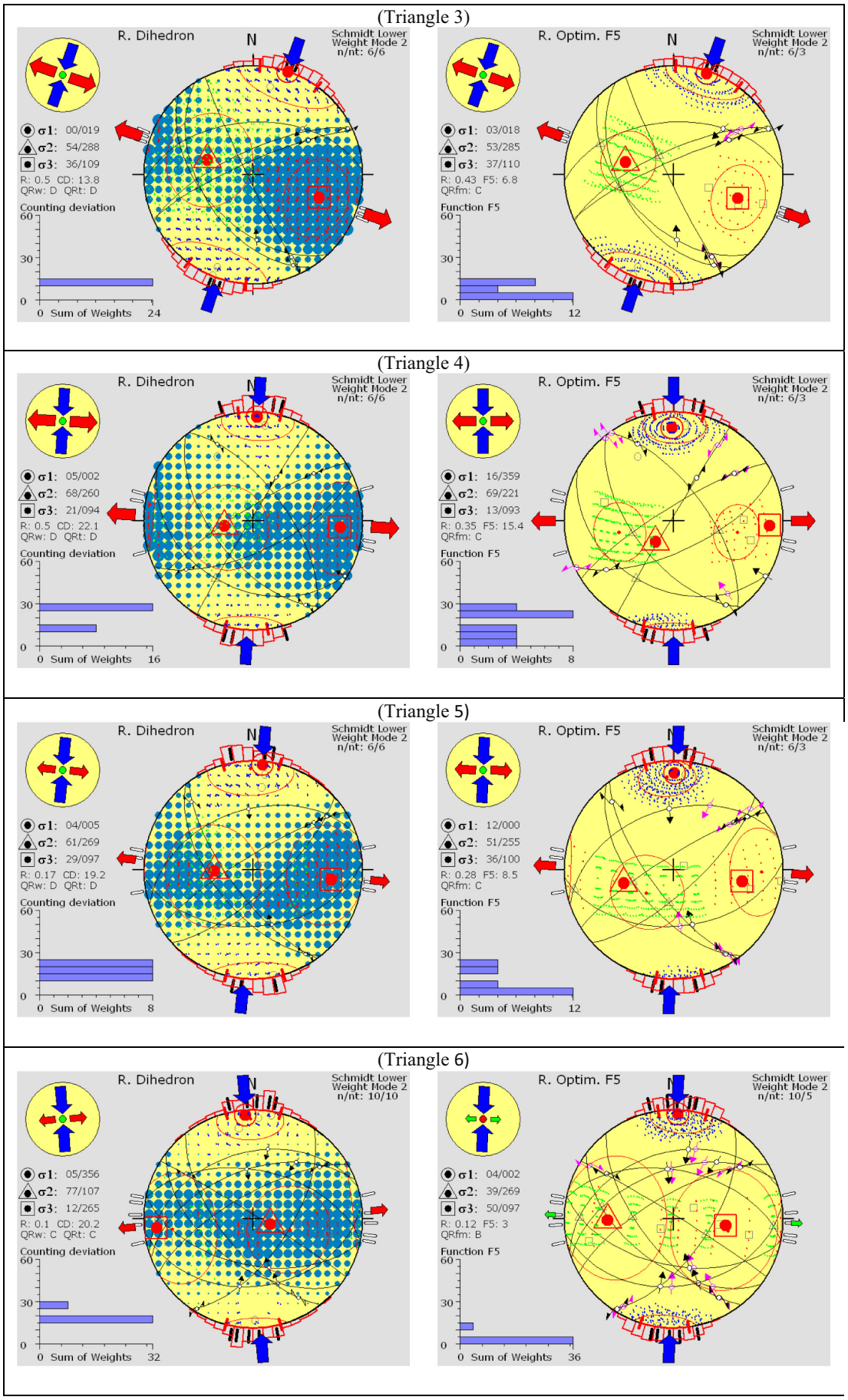

Fig. 4. The stress inversion resulted from the Rotational Optimization and Right Dihedral methods.

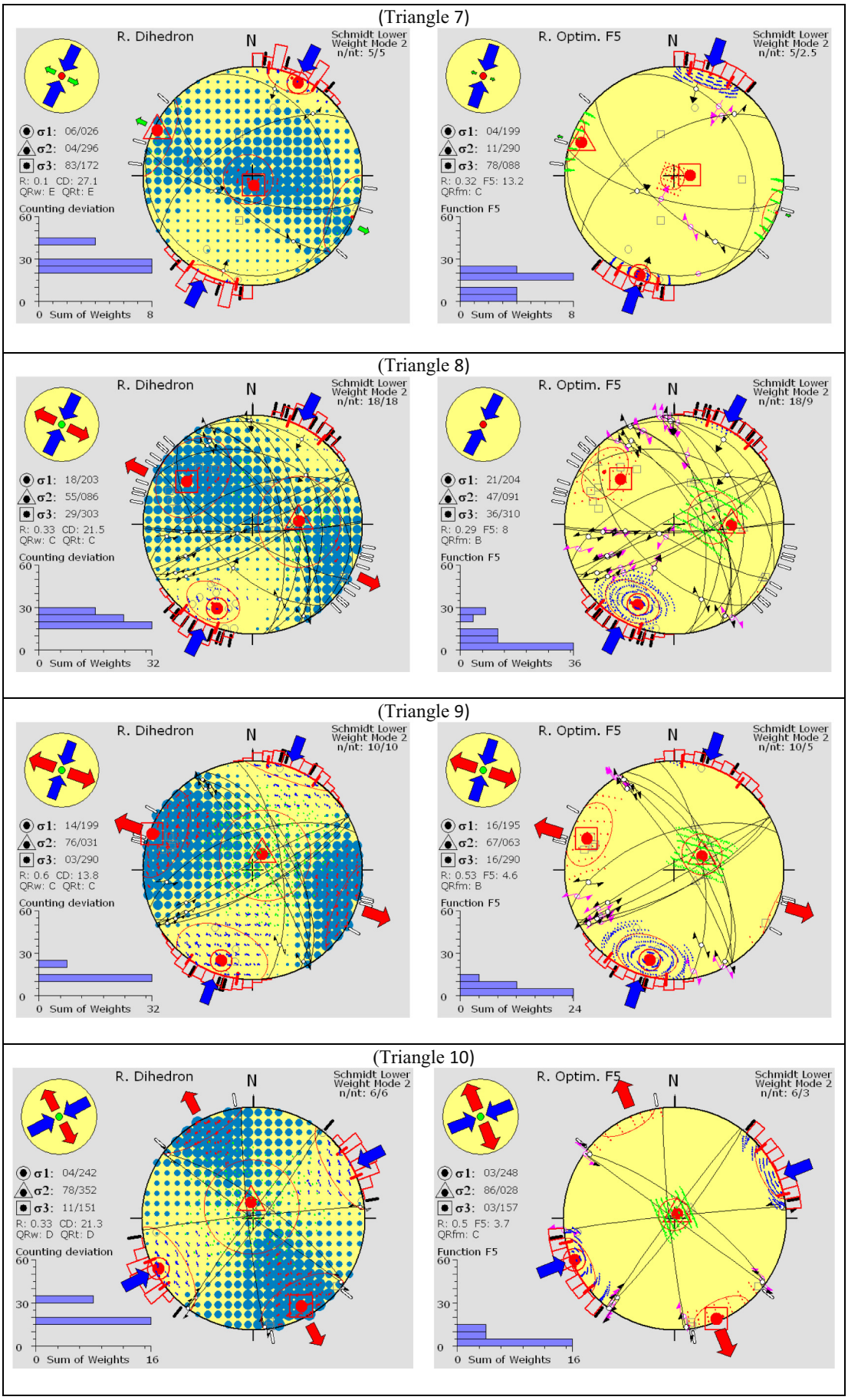

Fig. 4. (*continued*)

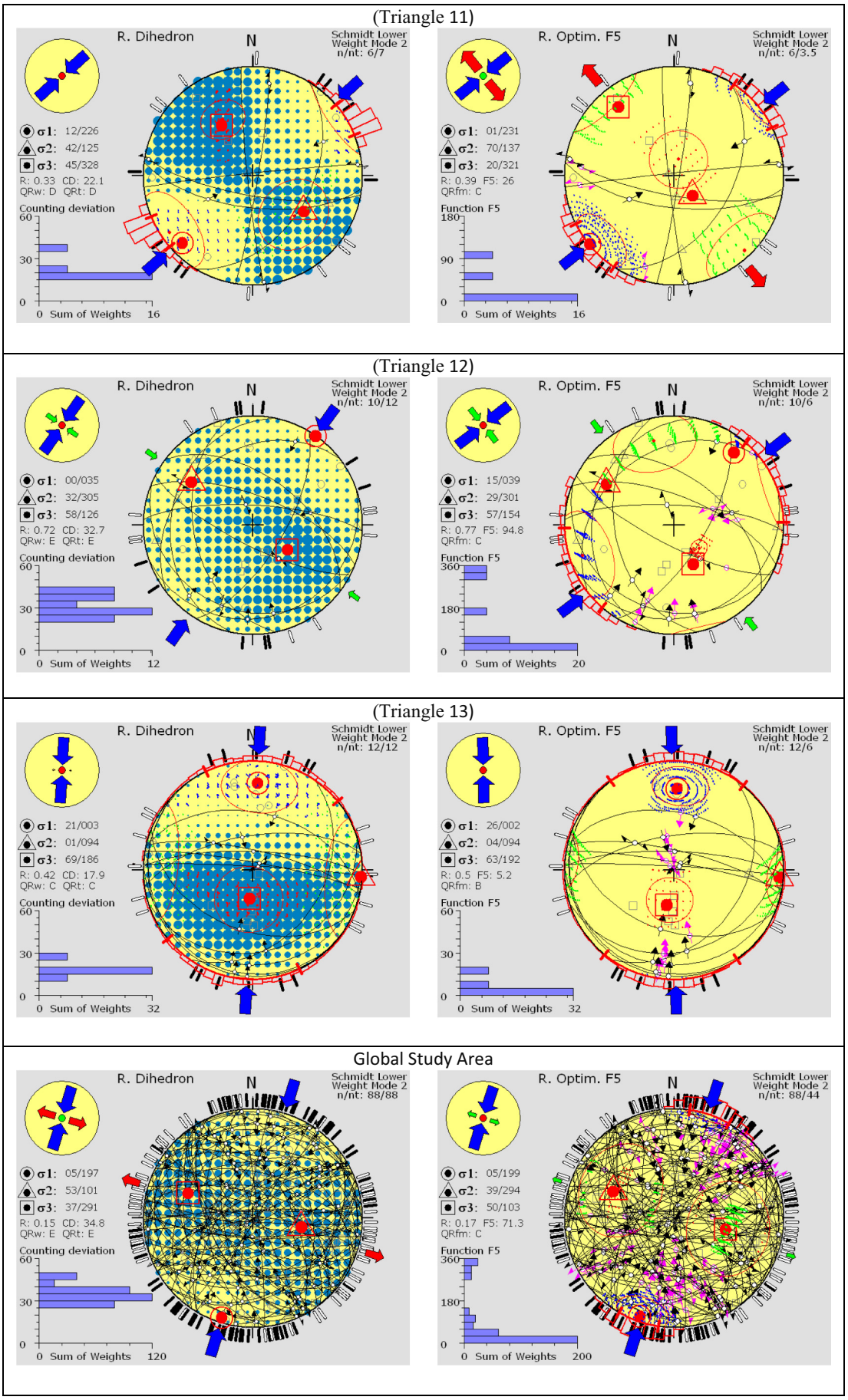

Fig. 4. (*continued*)

Table 3
The obtained present-day of the stress tensor parameters from the Rotational Optimization method for the triangular blocks (nt: the number of used data for the each block, σ_1, σ_2, σ_3: the directions of the main principal stress axes, R: the stress value, R′: the stress regime index, Sh_{min} and Sh_{max} are the azimuths of maximum and minimum axes of the seismic strain rate, respectively).

Triangular	n	nt	σ1	σ2	σ3	R	R′	SHmax	SHmin	Stress regime
3	6	3	03/018	53/285	37/110	0.43	1.57 ± 0.32	019 ± 17.6	109 ± 17.6	Compressional strike-slip
4	6	3	16/359	69/221	13/093	0.35	1.65 ± 0.25	000 ± 13.2	090 ± 13.2	Compressional strike-slip
5	6	3	12/000	51/255	36/100	0.28	1.72 ± 0.27	002 ± 12.1	092 ± 12.1	Compressional strike-slip
6	10	5	04/002	39/269	50/097	0.12	2.12 ± 0.26	002 ± 12.7	092 ± 12.7	Strike-slip compressive
7	5	3	04/199	11/290	78/088	0.32	2.32 ± 0.15	019 ± 11.1	109 ± 11.1	Strike-slip compressive
8	18	9	21/204	47/091	36/310	0.29	1.71 ± 0.29	28 ± 12.4	118 ± 12.4	Compressional strike-slip
9	10	5	16/195	67/063	16/290	0.53	1.47 ± 0.35	018 ± 16.4	108 ± 16.4	Compressional strike-slip
10	6	3	03/248	86/028	03/157	0.5	1.50 ± 0.41	068 ± 28	158 ± 28	Compressional strike-slip
11	6	4	01/231	70/137	20/321	0.39	1.67 ± 0.21	051 ± 15.3	141 ± 15.3	Compressional strike-slip
12	10	6	15/039	29/301	57/154	0.77	2.77 ± 0.23	031 ± 39.5	121 ± 39.5	Strike-slip compressive
13	12	6	26/002	04/094	63/192	0.5	2.5 ± 0.42	179 ± 37.3	269 ± 37.3	Strike-slip compressive
Total	88	44	05/199	39/294	50/103	0.17	2.17 ± 0.24	18 ± 11	108 ± 11	Compressional strike-slip

ε_{ij} and an asymmetric tensor ω_{ij}. This tensor can provide us with the differential rotation rate as its asymmetric parts (Eqs. (7) and (8)).

$$G_{ij} = \varepsilon_{ij} + \omega_{ij} \tag{7}$$

$$R_1 = \frac{-(\omega_{23} - \omega_{32})}{2},\ R_2 = \frac{-(\omega_{13} - \omega_{31})}{2},\ R_3 = \frac{-(\omega_{12} - \omega_{21})}{2} \tag{8}$$

R_i represents the amount of the rotation vector and the signs show the direction of rotations (The negative and positive signs indicate anticlockwise and clockwise rotations, respectively). Based on the differential rotations in each triangle (Table 7 and Fig. 7), the maximum and minimum rotation rates are 33.93 and 0.02 nanoradian/years, respectively. The largest amount of the rotation rates are observed in the

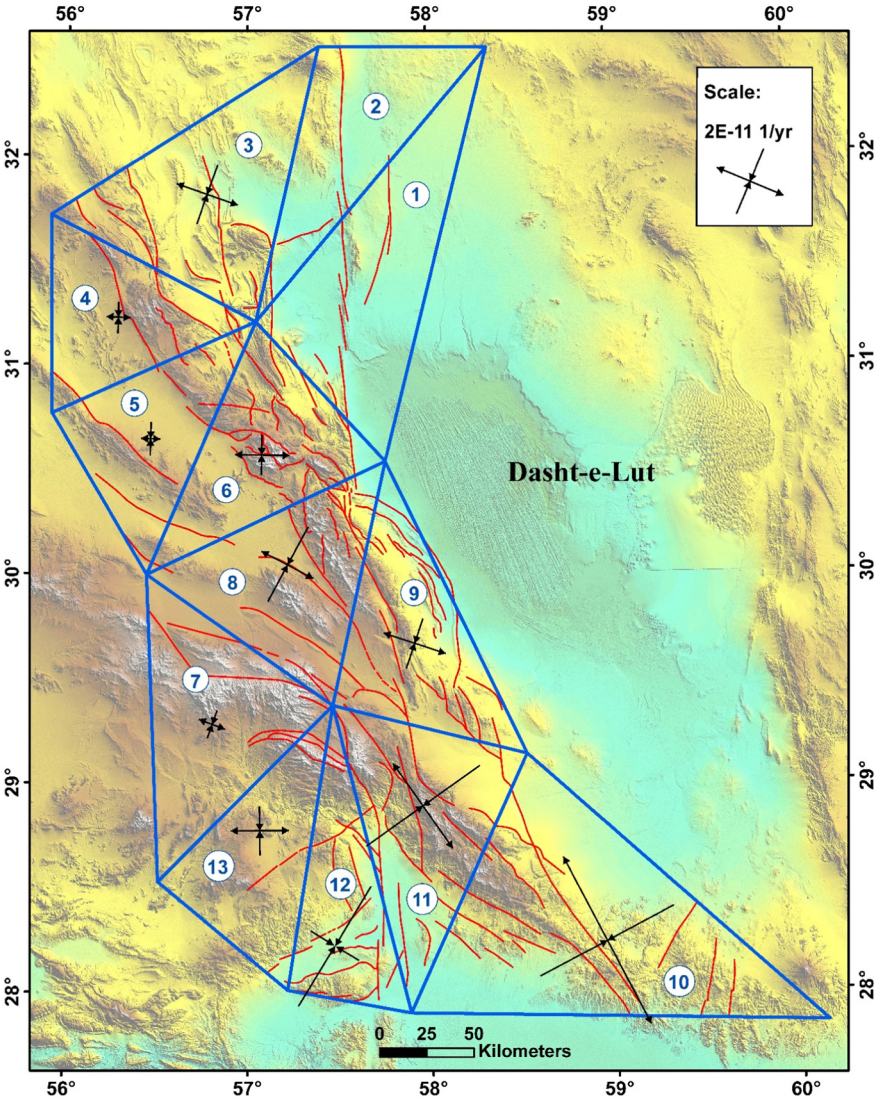

Fig. 5. The direction and relative magnitude of principal axes of the seismic strain rate in the study area.

Table 4
The values and azimuths of the axes based on the seismic strain rate.

Triangular	SHmax	Seismic Strain Rate (nanostrain/yr) for Shmax – compressional	SHmin	Seismic Strain Rate (nanostrain/yr) for Shmin - extensional
3	019 ± 17.6	−1.77527E−11	109 ± 17.6	1.81975E−11
4	000 ± 13.2	−8.91537E−12	090 ± 13.2	6.52096E−12
5	002 ± 12.1	−9.41039E−12	092 ± 12.1	4.11097E−12
6	002 ± 12.7	−1.12414E−11	092 ± 12.7	1.50856E−11
7	019 ± 11.1	−8.16149E−12	109 ± 11.1	7.18608E−12
8	28 ± 12.4	−2.45072E−11	118 ± 12.4	1.65343E−11
9	018 ± 16.4	−1.48287E−11	108 ± 16.4	1.81814E−11
10	068 ± 28	−4.31322E−11	158 ± 28	5.34682E−11
11	051 ± 15.3	−3.94158E−11	141 ± 15.3	2.92217E−11
12	031 ± 39.5	−3.96907E−11	121 ± 39.5	1.47827E−11
13	179 ± 37.3	−1.37467E−11	269 ± 37.3	1.60193E−11
Total	18 ± 11	−6.38078E−12	108 ± 11	5.82914E−12

triangles 11, 6, 9, 10, 1 and 12 in which there exist the main right-lateral strike-slip fault systems such as Sabzevaran, Gowk, Kuhbanan, Nayband, Bam, and Kahurak faults (Fig. 7). In triangle 7, where Lalehzar, Dalfard and Khordum faults are located and where western segments of Sabzevaran fault have a reverse mechanism with left-lateral strike slip, anti-clockwise rotation can be observed.

5. Analysis of the stress and strain fields

In order to investigate the relation between the strain and stress orientations, the results of earthquake focal mechanisms (FMSI), seismic strain rate (SSI) and geodetic strain rate (GSR) were compared. Fig. 8 illustrates the orientation of the compressional axes for each triangle resulting from each method. As the stress is continuously distributed through the study area, the stress and strain axes are similar in different triangles.

Similar to Zarifi et al. (2014), the correlation coefficient between the results of FMSI, SSR, GSR have been calculated and a new stress field was introduced using the related relationships.

Pearson's correlation coefficient indicates the correlation between the results from the stress inversion of focal mechanisms and those from the geodetic and seismic strain rate tensors. Pearson's correlation coefficient between two sets of variables are determined as the covariance of two variables divided by the product of their standard deviations (Gibbons and Chakraborti, 2011) as defined by Eq. (9):

$$p_{xy} = \frac{Cov(x,y)}{\sigma_x \sigma_y} \tag{9}$$

Pearson's correlation coefficient shows a measurement for the linear correlation between the two data collections in which Pearson's range (p) varies from −1 to +1.

Table 6
The maximum and minimum horizontal extension values with their azimuths.

Triangular	Max horizontal extension (e1H) (nano-strain/yr)	Azimuth of e1H (degrees)	Min horizontal extension (e2H) (nano-strain/yr)	Azimuth of e2H (degrees)
1	1.00897E−08	334.9628867	−2.7711E−08	64.9628867
2	9.24568E−09	307.0379016	−2.10655E−08	37.03790158
3	2.46225E−08	111.3904896	−1.692E−08	21.39048962
4	2.90181E−08	97.67311217	−1.15543E−08	7.673112169
5	2.68026E−08	270.7961042	−2.42321E−08	0.796104151
6	6.65387E−09	313.6897109	−1.98876E−08	43.68971089
7	1.75956E−08	313.1025491	−1.69618E−08	43.10254905
8	1.99408E−08	292.7637456	−4.57624E−08	22.76374559
9	3.30109E−08	304.2247754	−5.61471E−08	34.2247754
10	2.71576E−08	291.9513768	−2.82436E−08	21.95137676
11	3.08271E−08	305.8814668	−3.08022E−08	35.88146683
12	9.98052E−09	146.4789665	−3.00557E−08	56.47896655
13	−2.5995E−08	90.13546729	−7.85501E−09	0.135467286

Our results show an acceptable correlation between the obtained stress and strain tensors in the study area; p = +0.71 obtained for the correlation between FMSI and SSR, p = +0.71 for the correlation between the SSR and GSR, and p = +0.59 for the correlation between the FMSI and GSR. In addition, the mean direction of the compression stress (and strain rate) in each triangle, along with the absolute deviation value of each method of analyzing stress/strain tensor from the mean direction, were calculated. A new stress field in the study area is presented using the following weighted average (Eqs. (10), (11), (12)):

$$Weighted_{AVE} = \frac{Coef_{FMSI} \times FMSI + Coef_{SSR} \times SSR + Coef_{GSR} \times GSR}{Coef_{FMSI} + Coef_{SSR} + Coef_{GSR}} \tag{10}$$

$$\mathrm{Coef}_{\mathrm{Method}} = \frac{\sum \text{Dev. Methods} - |\text{Dev. from mean method}|}{\sum \text{Dev methods}} \tag{11}$$

$$\sum \text{Dev. methods} = |\text{Dev. from mean FMSI}| + |\text{Dev. from mean SSR}| + |\text{Dev. from mean GSR}| \tag{12}$$

Here | | show the absolute value and “Dev. from mean FMSI” represent the deviation of the FMSI result in each triangle from the mean value of the three methods, showing the direction of stress, in that triangle. The maximum weight is related to the method with the minimum deviation from the mean value and vice versa. Table 8 represents the results of the statistical approach. Fig. 9 shows the direction of the weighted average compression stress in the study area.

Table 5
The GPS velocities (Walpersdorf et al., 2014) used in this study.

Site	Lon	Lat	VE (mm.yr)	VN (mm.yr)	σ_{VE} (mm.yr)	σ_{VN} (mm.yr)	Span (years)	Sol.	Date midpoint
BAZM	60.18	27.865	5.33	3.11	2.06	1.62	6.02	3	2001.6115
SORC	57.884	27.901	0.94	12.57	1.44	1.43	1.99	4	2001.953
GHOL	57.217	28.01	2.12	15.01	1.03	0.95	1.99	4	2001.9282
DENA	56.504	28.529	4.05	14.69	1.45	1.44	1.99	2	2001.9122
BA12	58.523	29.137	2.6	7.19	1.03	1.03	3.87	8	2007.666
HSAD	57.465	29.371	1.8	13.78	1.56	1.56	1.73	2	2007.7626
BRSR	56.445	29.997	−0.12	14.6	1.66	1.65	1.73	2	2007.253
CMCV	57.76	30.537	0.36	8.2	1.61	1.6	1.73	2	2007.5926
IRAJ	55.929	30.775	−0.87	12.89	1.58	1.58	1.73	2	2007.5479
ABJN	57.046	31.206	2.3	10.9	1.62	1.62	1.73	2	2007.684
SEND	55.929	31.713	−0.52	11.75	1.04	1.04	3.87	5	2007.5585
ABGR	58.319	32.484	0.77	7.09	1.57	1.57	1.73	2	2007.7432
NYBD	57.397	32.492	0.92	8.81	1.25	1.26	2.63	3	2008.6343

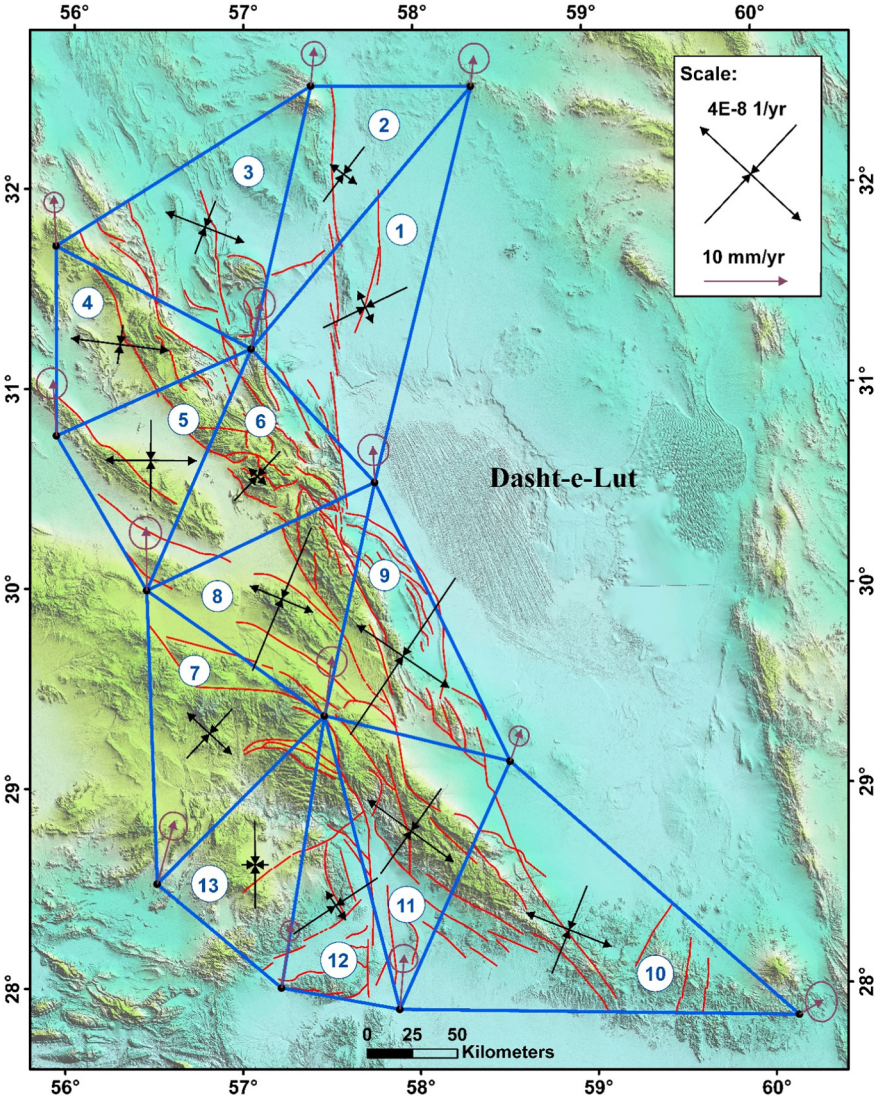

Fig. 6. The GPS velocity field with their error ellipses relative to the Eurasian as a fixed reference frame, the active faults and Delaunay triangles. The principal geodetic strain rates (black) obtained from the GPS velocities (red). (For interpretation of the references to color in this figure legend, the reader is referred to the web version of this article.)

Table 7
The geodetic rotation rate in triangular networks.

Triangular	Rotation (degrees/yr)		Rotation (nano-rad/yr)		Direction of rotation
	Amount	± uncertainty	Amount	± uncertainty	
1	1.22E−06	0	+21.3296	0.0825	Clockwise
2	3.04E−07	1E−8	+5.3015	0.1019	Clockwise
3	1.34E−09	0	+0.0233	0.0737	Clockwise
4	4.94E−07	1E−8	+8.4609	0.0891	Clockwise
5	4.11E−07	1E−8	+7.1966	0.0915	Clockwise
6	1.94E−06	0	+33.9371	0.084	Clockwise
7	−4.77E−07	0	−8.3478	0.077	Anti-clockwise
8	5.81E−07	0	+10.141	0.0773	Clockwise
9	1.68E−06	0	+29.2986	0.0861	Clockwise
10	1.30E−06	0	+22.6441	0.0557	Clockwise
11	2.12E−06	0	+37.0408	0.0793	Clockwise
12	1.10E−06	1E−8	+19.1261	0.1161	Clockwise
13	1.15E−07	1E−8	+1.9361	0.0929	Clockwise

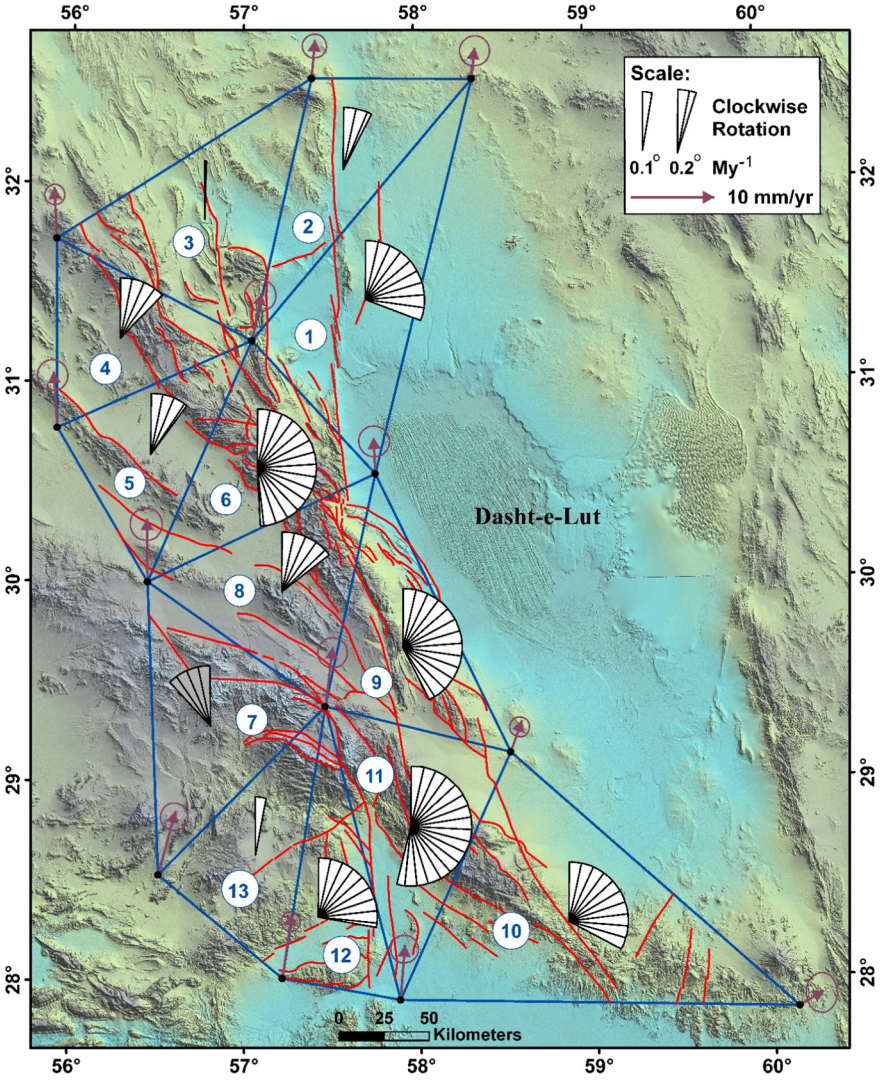

Fig. 7. The geodetic rotation rate along with GPS velocities (red). (For interpretation of the references to color in this figure legend, the reader is referred to the web version of this article.)

6. Geodetic and seismic moment rates

The geodetic and seismic moment rates were calculated using the results of Ward (1998) and Pancha et al. (2006). For the hazard analysis purposes, this new information has been considered in comparison with the geodetic and seismic strain rates.

As the moment rates are related to the amount of accumulated and released energy, we can get useful information about the fault activities and their seismic risks. We used ArcGIS software to map the geodetic and seismic moment rates. The ArcGIS Spatial Analyst offers several interpolation tools for generating surface grids from point data (Childs, 2004). Some of them are the IDW, Spline, and Kriging interpolation methods. Each method uses a different approach for determining the output network values. The most appropriate method will depend on the distribution of sample points and the phenomenon being studied. We used the Kriging interpolation which is a powerful statistical method (Childs, 2004). It fits a function to a specified number of points or all points within a specified radius to determine the output value for each location.

6.1. Geodetic moment rate

The geodetic moment rates represent a part of the interseismic deformation which takes place in the area and can be obtained using the GPS velocities. In this study, the geodetic moment rates are calculated in each triangular network following Kostrov (1974) procedure (Eq. (13)).

$$\dot{M} = 2\mu A H_S \dot{\varepsilon} = (1/T) \sum_{n=1}^{m} M_n \quad (13)$$

where μ, A, and Hs are the rigidity, the network area and the seismogenic thickness, respectively. Using the known values of T, A (Table 9), μ (3×10^{10} Pa) and Hs (15 km), the geodetic monitoring can be quantified into potential seismic activities within the network even if the activity is related to unknown faults or those with too slow slip which difficult to study by conventional geological or seismological techniques.

Based on our calculations, the geodetic moment rates in some triangles such as 1, 8, 9, 12, and 13 are more than other ones (Table 9). There are folds, faults with high seismic activity history (such as the south segment of Nayband, north segments of Gowk, North Faryab, Chahmazrae faults) in these triangles.

In most parts, the geodetic moment rates are consistent with high seismicity (Fig. 10). However, in the south of the Lut block (Jabal-e Barz), despite the occurrence of numerous earthquakes, the geodetic moment rate is low which can be possibly assigned to the type of rock units which are igneous rocks (Firouzkouhi et al., 2017; Ghodsi et al.,

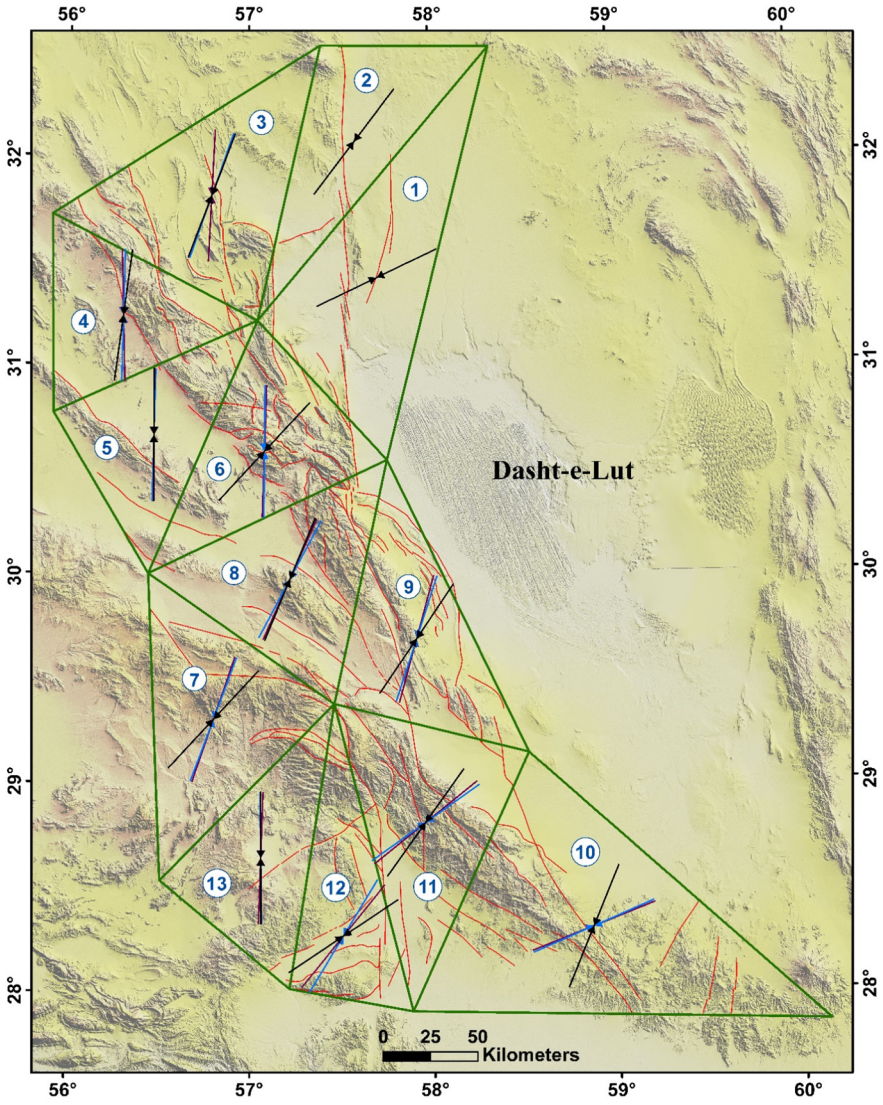

Fig. 8. The comparison between the principal axes directions extracted from the stress inversion (red), the seismic strain rates (blue) and the geodetic strain rates (black) in the study area. (For interpretation of the references to color in this figure legend, the reader is referred to the web version of this article.)

Table 8
The weighted average of maximum horizontal compression axes obtained from the FMSI, SSR and GSR methods.

Triangular	Mean value of azimuth	Dev. from mean (FMSI)	Dev. from mean (SSR)	Dev. from mean (GSR)	Weighted average azimuths
3	19.46	1.46	0.46	1.92	12.08
4	2.55	2.55	2.55	5.11	10.03
5	0.93	0.93	1.06	0.13	5.28
6	15.89	13.89	13.89	27.79	19.03
7	27.03	8.03	8.03	16.06	18.88
8	24.92	0.92	3.07	2.15	19.18
9	22.4	7.4	4.4	11.81	15.18
10	52.65	15.34	15.34	30.69	48.37
11	45.96	5.03	5.03	10.07	39.1
12	42.15	3.15	11.15	14.31	34.32
13	0.71	1.28	0.71	0.57	8.38

2016; Rasouli et al., 2016).

6.2. Seismic moment rate

In this study, all earthquakes from 1900 through 2015 were used to calculate seismic moment rates (Fig. 11). The amount of seismic moment for each earthquake can be obtained using its magnitude (Eq. (14)).

$$\mathrm{LogM0} = \mathrm{Cm} + \mathrm{d} \tag{14}$$

where m is the magnitude, M0 is the seismic moment; C and d are constant parameters associated with the Hanks & Kanamori law (Hanks and Kanamori, 1979).

We obtained the seismic moment for the study area (Fig. 12). The maximum amount of released energy is occurred in the years 1981, 1998, 2003, 2010, 1911, 2005 and 2011 in which the main earthquakes occurred (Table 10).

There are two ways which can be used for converting the seismic moment to the seismic moment rate: using the cumulative seismic moment diagram (Pancha et al., 2006) and the average seismic moment of earthquakes (Ward, 1998). We used both methods to calculate the seismic moment rate (Table 11).

The maximum seismic moment rates are observed in triangles 9, 10, 8, 13, and 11 (Table. 11; Fig. 13) where the main faults are the Gowk, Shahdad, Bam, Kahourak, Jebal-e barez, Mahan, East Kerman, North Faryab, Chahmazrae, branches of Kuhbanan, and Jorjafk faults. Some faults with high slip rates such as Sabzevaran and Nayband faults had a significant contribution to the resulting seismic moment rate.

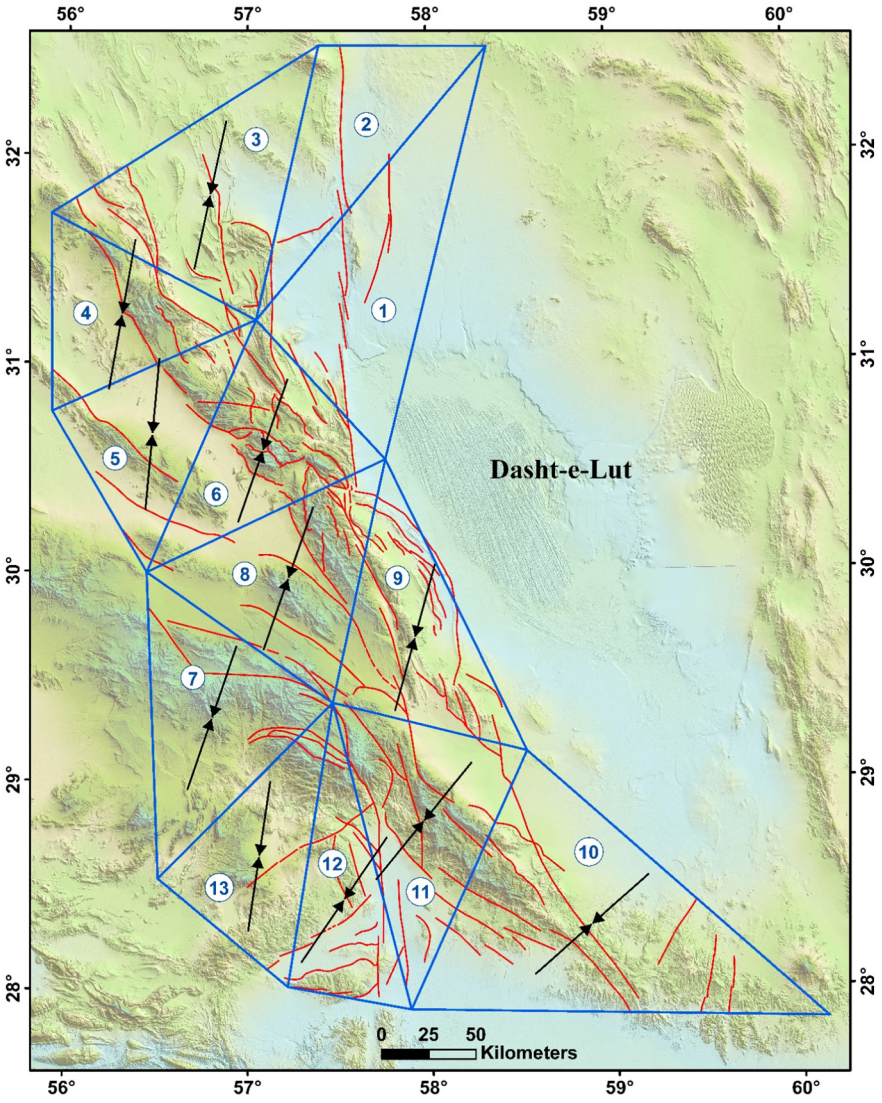

Fig. 9. The obtained direction of the weighted average of maximum horizontal compression stress from FMSI, SSR and GSR.

Table 9
The maximum principal amount of the strain rate tensor and the geodetic moment rates for each triangular network in the study area.

Triangular	Area (km^2)	Maximum principal amount of strain rate tensor	$\dot{M}$ = geodetic moment rate (Nm/yr)
1	9481.219	17.6213	1.50E+17
2	6457.478	11.8198	6.87E+16
3	8824.701	7.7025	6.12E+16
4	5682.754	17.4638	8.93E+16
5	5838.778	2.5704	1.35E+16
6	6725.562	13.2337	8.01E+16
7	7823.083	0.6338	4.46E+15
8	7344.951	25.8215	1.71E+17
9	7011.477	23.1362	1.46E+17
10	15,330.827	1.0861	1.50E+16
11	7852.91	0.0249	1.76E+14
12	5092.909	20.0752	9.20E+16
13	5893.235	33.85	1.80E+17

The amount of geodetic moment rates for triangles 13, 8, 1, 9, and 12 and the seismic moment rates in 9, 10, 8, 13, and 11 ones are significant (Fig. 14).

7. Discussion

7.1. Tectonic analysis of the study area

Studies on active tectonics in the west and south of the Dasht-e Lut (Fig. 1) indicate the important role of the strike slip and reverse faults in this part of Iran. The large portion of the 15 mm/yr NS slip rate between Afghanistan and Iran blocks (interior of Iran) accumulate on the faults in the west of the Lut block such as Nayband, Gowk, Sabzevaran, and Kuhbanan faults (Foroutan et al., 2014; Kermani et al., 2017; Meyer and Le Dortz, 2007; Rahbar et al., 2017; Vernant et al., 2004; Walker et al., 2010). The current stress in the west of the Lut block causes shearing and the directions of the compressional stress are approximately NS which agrees with previous studies (e.g. Zarifi et al., 2014).

The southern part of the study area is the transition zone between the Zagros, Central Iran and Makran (Fig. 1). Different researchers have discussed the structural evolution of this area (Agard et al., 2005, 2007, 2011; Aubourg et al., 2008; Derakhshani and Farhoudi, 2005; Rahnamarad et al., 2008; Regard et al., 2006, 2010). Aubourg et al. (2008) illustrated the structures with respect to the convergence

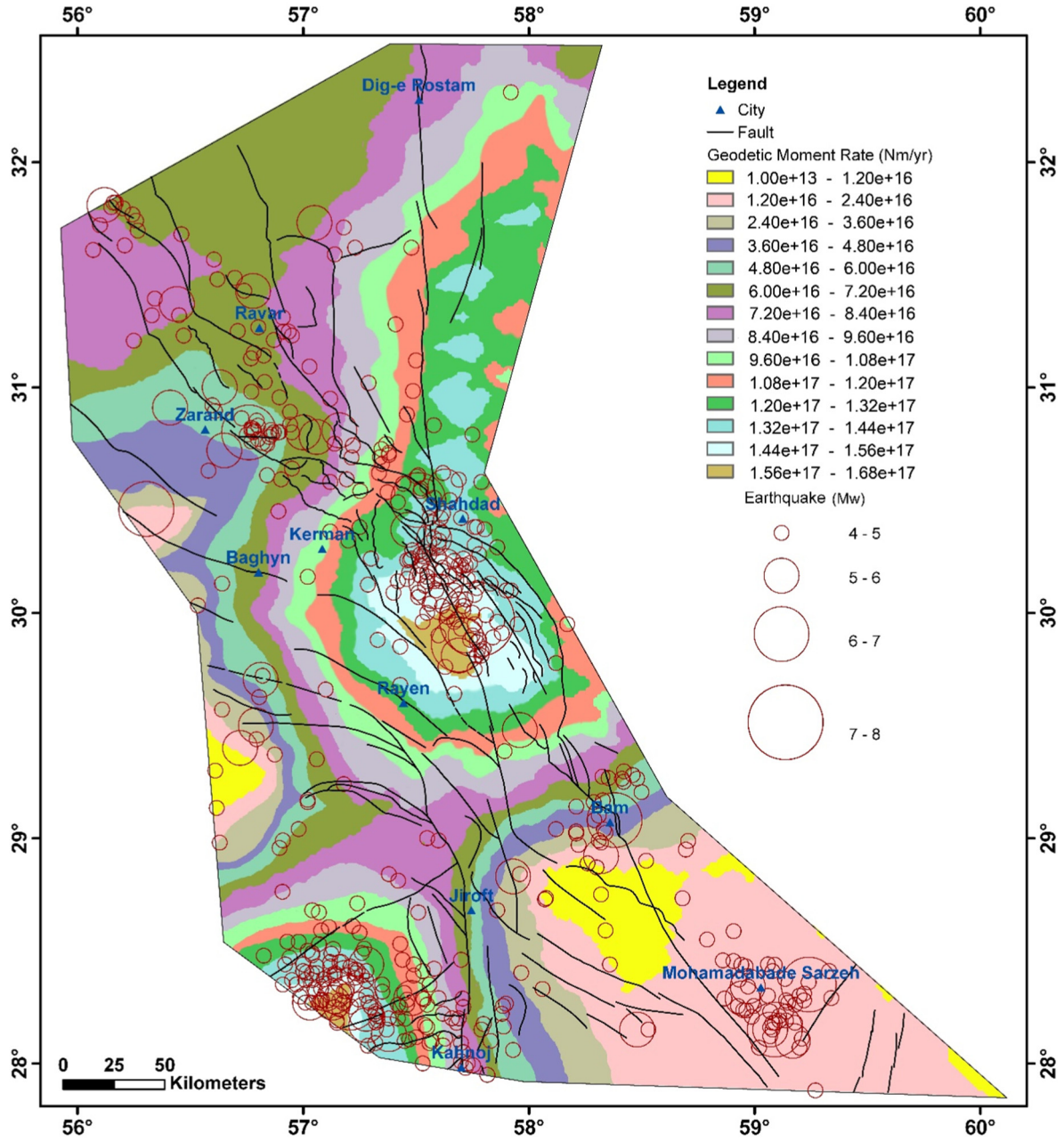

Fig. 10. The geodetic moment rates overlaid by earthquake distributions in the study area (1900–2015).

direction of Arabia relative to the Iranian plate. The asymmetry between the western and eastern parts of the Fars Arc in the Zagros Makran Syntaxis (ZMS in Fig. 1a) corresponds to shear zones proposed by Aubourg et al. (2004), in the hypothesis of the Oman peninsula acting as an indenter. Our directions of horizontal compression stress obtained in the study area (Fig. 9) are consistent with their structural studies.

The comparison of seismic and geodetic strain rates marks the zones of higher seismic deformation and can be correlated with the distribution of large earthquakes. For earthquake hazard assessment, we divided our study area into 13 triangular networks (Fig. 2). We obtained the geodetic and seismic strain and moment rates and we investigated the role of these parameters in the seismicity of the study area.

The geodetic strain rate in the triangles 8, 9, 10 and 11 are larger than the other ones (Fig. 6). These results are in line with the model that the slip is transferred from the main southern fault, Sabzevaran, to the faults in the northern part such as Gowk by Oman peninsula acting as an indenter. From 1977 to 2012, ten destructive earthquakes were accompanied by about 185 km of the surface rupture in along these faults and their branches (Fig. 2 & Table 1). These earthquakes resulted in ~44,700 human loss, and ~36,646 injured. Eight of them have occurred in the triangles 8, 9, 10 and 11 that show high geodetic strain rates (Fig. 6). Five earthquakes, 1981/06/11 (Mw 6.6), 1981/07/28 (Mw 7.1), 1989/11/20 (Mw 5.8) 1998/03/14 (Mw 6.6) and 1998/11/18 (Mw 5.3), occurred along the northern part of the Gowk fault inside triangles 8 and 9 (Fig. 2; nos. 10, 11, 15, 35, 39). The devastating Bam earthquake (2003/12/26; Mw 6.6) occurred due to the activity of the Bam fault system, which is situated in the boundary of the two triangles 10 and 11 (Fig. 2; no. 32). The South Rigan earthquake sequence (2010/12/20; Mw 6.5 and 2011/01/27; Mw 6.2) occurred along right-lateral strike-slip and left-lateral faulting (Fig. 2; nos. 29, 30). These faults are located inside triangle 10. The triangles 10 and 11 are located in the transitional zone between the Zagros and Makran and they are

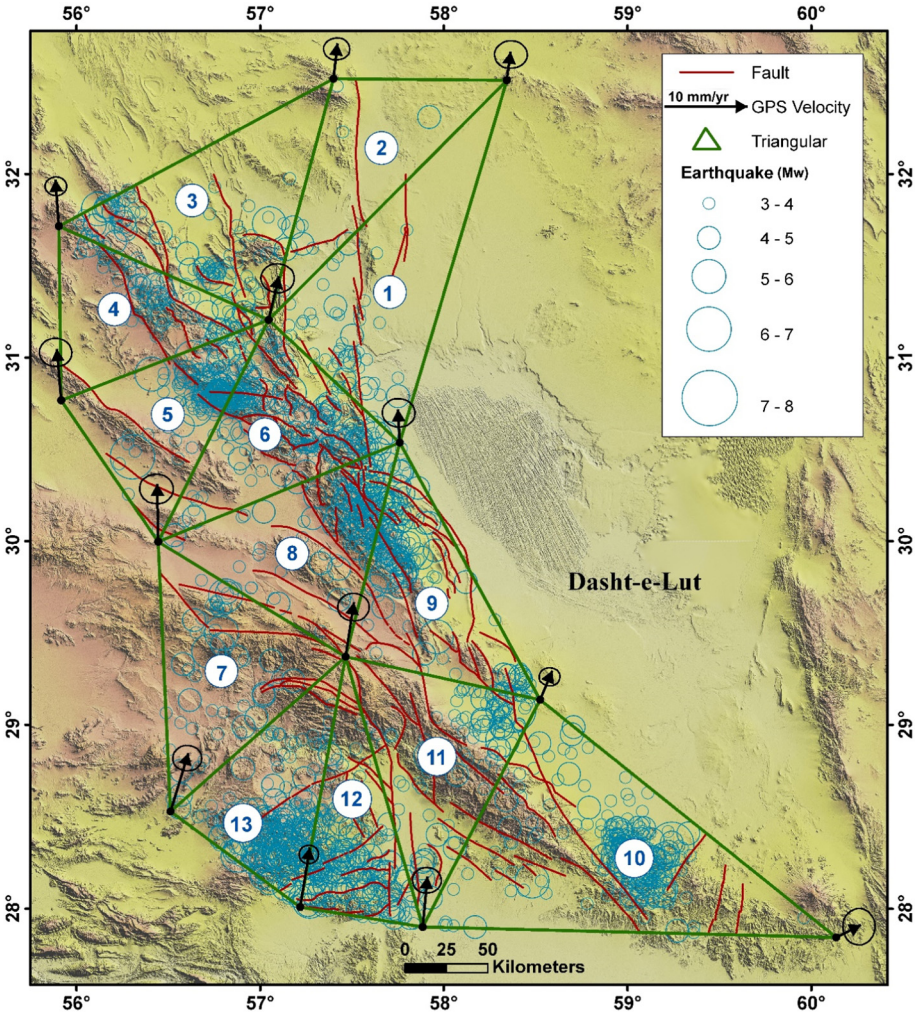

Fig. 11. The triangulated networks of the study area with the main faults and earthquake distribution from 1900 through 2015.

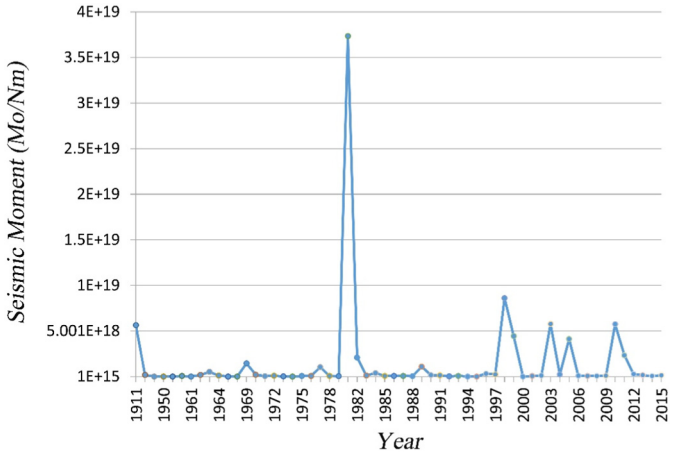

Fig. 12. The seismic moment changes for the study area through1900 to 2015.

near to the stress fields introduced by indentation tectonics. In addition to these earthquakes more instrumental earthquakes occurred in these parts of the study area (Fig. 11). The results of the moment rates also show large energy released in the triangles 10 and 11 (Fig. 14).

We also estimated the seismic strain rate for each triangle. Each earthquake was assigned as a scalar moment obtained from the catalogues. As such, we expect to account for most of the seismically strain released. Each triangle may cover zones of different style of deformations and the Kostrove's summation averages.

Table 10
Destructive earthquakes, with the high seismic moment, in the study area in the period of 1900 to 2015.

ID	Date		Earthquake name	Mw	Seismic moment (Nm)
1	1981	1981.07.28	Sirch	7.1	3.73479E+19
		1981.06.11	Golbaf	6.6	
2	1998	1998.11.18	Chehar Farsakh	5.3	8.60273E+18
		1998.03.14	Fandoqa	6.6	
3	2003	2003.12.26	Bam	6.5	5.75762E+18
4	2010	2010.07.31	Lalehzar	5.7	5.74095E+18
		2010.12.20	Mohamad Abad Rigan	6.7	
5	1911	1911.04.19	Ravar	Mb = 6.7	5.62341E+18
6	2005	2005.02.22	Dahueiyeh	6.4	4.13174E+18
7	2011	2011.01.27	South Mohamad Abad Rigan	6.2	3.62341E+18

Triangles 8 and 9, in the middle of the study area, show more different patterns for the large and small earthquakes (Fig. 2). Earthquakes indicate North-South shearing in the west of the Lut block. As expected, the geodetic strain corresponds to the combination of the large and small earthquake deformation.

In the study area, directions of the seismic strain rate are coaxial with directions of the geodetic strain rate even if its amplitude is small (Fig. 8). This consistency between geodetic and seismic strain rate

Table 11
The seismic moment rate in the triangular networks of the study area.

Triangular	Seismic moment rate using average seismic moment of earthquakes (Nm/yr)	Seismic moment rate using chart of cumulative seismic-moment (Nm/yr)
1	1.7407E+15	1E+15
2	2.67126E+14	2E+14
3	4.71522E+15	4E+15
4	4.62185E+15	5E+15
5	1.03949E+17	1E+17
6	5.19393E+16	6E+16
7	4.93766E+15	3E+15
8	1.57851E+17	2E+17
9	7.47538E+17	8E+17
10	2.19934E+17	1E+17
11	1.0985E+17	2E+17
12	1.8216E+16	2E+16
13	1.14003E+17	1E+17

directions implies that the continuous or discontinuous assumptions used for computing the style and strain rate direction lead to the same conclusions. Indeed, geodetic strain corresponds to continuous deformation inside a triangle, and seismic strain is computed with the discontinuous deformation due to displacements along faults. In a few triangles, the ratio of the seismic and geodetic strain rates is slightly different. Two of these triangles correspond to the triangles discussed in Fig. 8, where the seismic strain deduced from the large and small earthquakes is different. Summarizing the geodetic and seismic style and direction of deformation, we observe that the southern border of the Lut block is characterized by a compressive strain orientated about N45° (Fig. 9). It could be due to the existence of the Oman peninsula, which plays a major role in the tectonic regime in the south of the study area. The triangles 10, 11 and 12 also show high seismic strain rate where the main faults are the Sabzevaran, Jebal-e Barez, Bam, Kahourak faults (Fig. 5). The Sabzevaran fault has a maximum slip rate of 5.7 ± 1.7 mm/yr (Regard et al., 2006). Since a part of the deformation is accommodated by the numerous thrusts in the western compartment (Rashidi Boshrabadi et al., 2018), so the overall strike-slip motion accommodated by the Nayband-Gowk system is decreasing from the South to the North. The obtained stress regimes and the compression stress direction, in the different parts of the study area (Table 3 & Fig. 9) are consistent with dip-slip and strike-slip faulting on known active faults.

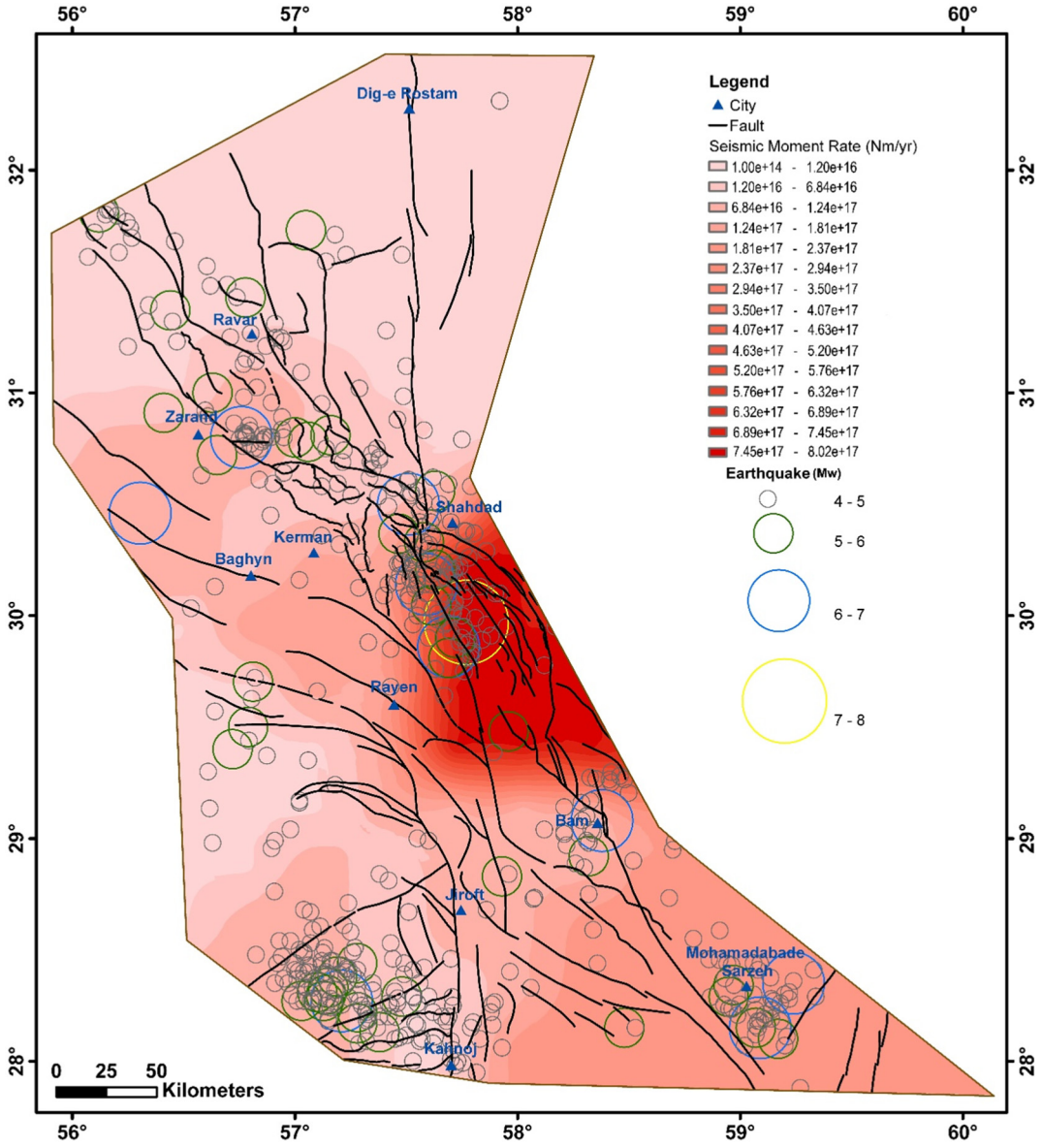

Fig. 13. The seismic moment rate with earthquake distribution in the study area (1900–2015).

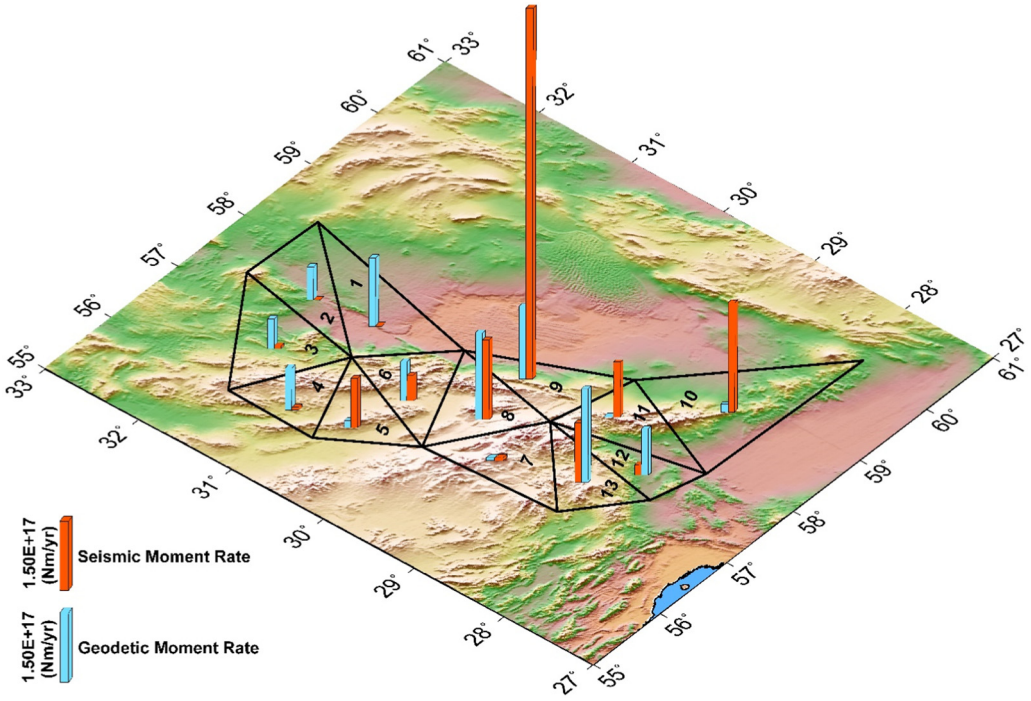

Fig. 14. The geodetic and seismic moment rates in the study area.

The difference in the seismic strain rate in different parts of the study area is surprisingly consistent with the number of main earthquakes. There is a strong global correlation between relative geodetic moment rates (in different areas) and particularly the relative number of earthquakes. The amount of the geodetic moment rates for triangles 13, 8, 1, 9, and 12 and also the seismic moment rates in triangles 9, 10, 8, 13, and 11 are relatively significant (Fig. 14). The ratio of the seismic to geodetic moment rate shows the lowest values for triangles 2, 1, 4, and 3 with the high ones for triangles 10 and 11. The higher released energy observed in triangles 10 and 11 can be related to the presence of the igneous brittle rocks in this area where the southeast part of the Urumieh-Dokhtar volcano-Plutonic belt (the Jebal-e Barez mountain ranges) and the southwest part of the Makran Volcanic Arc (the Bazman volcanic field) are located in this area (Firouzkouhi et al., 2017; Ghodsi et al., 2016; Rasouli et al., 2016). According to the geodetic and seismic moment rates, the seismic hazards in triangles 1, 8, 13, 9, 5, and 6 are high.

The Gowk, Bam, Kahourak, North Faryab and Kuhbanan fault systems released a large amount of seismic energy during recent years. In contrary, the Sabzevaran and Nayband faults (in Fig. 1c) are the two main fault systems in the study area where the seismic moment rate is low (Fig. 13). Geomorphological evidence shows the high activity of these faults (Hashemi et al., 2018; Meyer and Le Dortz, 2007; Regard et al., 2005) in which the high probability of large earthquakes along them can be expected. The anomalously low seismicity rate along the major strike-slip faults is due to this fact that along these fault zones (such as the Sabzevaran and Nayband fault systems) the magnitude frequency relationship is better approximated using a characteristic earthquake distribution instead of the more general Gutenberg-Richter relationship (Wesnousky, 1988). The characteristic earthquake model adequately describes the relatively high occurrence probability of large events compared with the small ones.

Generally, comparing the seismic and geodetic moment rates indicates the highly strained zones experience mainly aseismic deformation in the northern part of the study area and seismic deformation in its middle and southern parts (Fig. 14). Especially, high seismic coupling zones correlate well with high magnitude earthquakes zones.

The Pleistocene and Holocene right-lateral slip rates along the western margin of the Lut block, at longitude ~57°45′ E, increases from the north toward the south. This southward increment activity, which indicates the complexity of the structural evolution, is inferred from the slip rates of the Nayband, 1.8 ± 0.7 mm/yr (Foroutan et al., 2014); Gowk, 3.8 ± 0.7 mm/yr (Walker et al., 2010) and Sabzevaran faults, 5.7 ± 1.7 mm/yr (Regard et al., 2006). In the study area, the released energy is directly related to the active fault slip rates. In the active tectonic zones, the seismic and interseismic deformation is linked to the structural evolution of faults with different slip rates.

In the study area, the Ravar, Takdar, Behabad, Kuhbanan, Jorjafk, East Kerman, Gowk, Bam, Kahurak, and Sabzevaran faults are the main systems (Fig. 1c). According to the obtained tectonic stress parameter (R'), the right-lateral component dominates over the reverse one in most parts (Table 3 & Fig. 3). However, in some parts, the reverse component dominates over right-lateral one where the main faults are the southern segments of the Kuhbanan fault (Dahueiyeh Fault), Sardueiyeh, Lalehzar, Dalfard, Khordum, South Faryab, Heydarabad, and North Faryab faults (Fig. 1c).

7.2. Comparison of the results with other tectonic regions

The obtained results in our study can be compared with the similar tectonically active regions in other parts of the world. Gupta et al. (2015) reported the extensive compression and shortening in the direction of indentor convergence in the eastern Himalayan Syntaxis (EHS). They analyzed the strain rate tensor based on the horizontal velocities. The obtained largest component of deformation in the EHS area has been explained by the existence of a series of N-S strike-slip faults. In Tibetan plateau, the rotation rate increases from the west to the east where the transfer of motion from the west to the east takes place and the shortening component rotates roughly from the N-S to the NE-SW in which accommodates the motion around the indentor. The maximum of the compression rates is created by the transfer zone of the main right lateral motions (Bame-Tutin Fault). Norabuena et al. (2004) interpreted the seismogenic zone, based on the seismic and geodetic data, in Central America where the Cocos and Caribbean plates converge. In Nicoya, the GPS information suggests two locked patches centered at 14 ± 2 and 39 ± 6 km depths. The concentration of

Table 12
The seismic/geodetic moment rates ratio with other parameters for our study area and other regions.
(Ward, 1998; Pancha et al., 2006)

Regional	Area km^2	$\dot{M}_{geodetic}$ 10^{19} Nm/yr	$\dot{M}_{seismic}$ 10^{19} Nm/yr	Hs km	$\left[\frac{\dot{M}_{seismic}}{\dot{M}_{geodetic}}\right]$%
Study area	0.993×10^5	1.07	0.154	~15	14.4
USA	7.945×10^6	4.58	3.62	~11	79
S.Calif	0.15×10^6	1.23	1.06	~11	86
N.Calif	0.240×10^6	0.89	0.66	~11	74
Basin & range	0.775×10^6	1.08 0.39–0.69	0.55 0.58–1.12	~11	51
Northwest	1.027×10^6	0.72	0.18	~11	25
Central	2.730×10^6	0.52	0.013	~15	2.5

interplate microseismicity in the more freely slipping intermediate zones suggests the small interseismic earthquakes may not accurately outline the up-dip limit of the seismogenic zone, the rupture zones for the future large earthquakes.

The results of the seismic/geodetic moment rates ratio for our study area, 14.4%, is comparable to the results suggested by previous studies for the United States (Ward, 1998) and the Basin and Range (Pancha et al., 2006) (Table 12). The seismic/geodetic moment rate ratio indicates that 14.4% of the region's fault energies have been released and much of the elastic energy has not been released yet. This ratio in our study area is lower than what was obtained for the United States and Basin & Range (Ward, 1998 and Pancha et al., 2006) and indicates the high seismic hazard in our study area relative to those regions.

8. Conclusions

The new obtained stress map was established using the focal mechanisms formal inversion and analysis of the geodetic data for the western and southern of the Lut block. The results show a good correlation between the direction of the principal components of FMSI, SSR, and GSR. Our new analysis in the west and south of the Lut block were compared with the mechanism of the main faults which have been represented by the previous studies (Walker et al., 2010; Allen et al., 2011; Fattahi et al., 2011; Foroutan et al., 2014 and Rashidi Boshrabadi et al., 2018).

The obtained orientation of the mean stress using the FMSI data in the west and south of the Lut block is about N19 E (Fig. 4) with a compressional strike-slip tectonic regime. In the study area, data analyses indicate the existence of three categories of the stress regimes including strike-slip (43.2%), thrust (38.6%), and unknown or oblique faultings (18.2%).

The calculated rotation rates using the GPS velocities (Fig. 7) show the maximum amount of rotation rate around the right lateral strike slip faults such as the Sabzevaran, Gowk, Nayband, Bam, Kuhbanan, and Kahurak faults.

The ratio of seismic moment rate/geodetic moment rate in the south of the Lut block is high (Fig. 14) due to the presence of igneous brittle rocks in which more energy is released. According to the geodetic and seismic moment rates, the seismic hazard along the southern segment of the Nayband, Mahan, Rayan, North Faryab, Gowk, Kuhbanan, and Lakarkuh faults are higher.

Acknowledgements

This work was supported by International Institute of Earthquake Engineering and Seismology (IIEES). We are grateful to the editor, Philippe Agard, for his useful and constructive comments on earlier versions of this manuscript. We thank three anonymous reviewers for helpful reviews and Hamid Zafarani (the IIEES faculty) for peer reviewing the manuscript and constructive comments. The authors are greatly indebted to DamiEn Delvaux of the Royal museum for Central Africa for giving us the permission to use the Win-Tensor software. GMT, ArcGIS and ZMAP free software/programs were used in this study.

References

Agard, P., Omrani, J., Jolivet, L., Mouthereau, F., 2005. Convergence history across Zagros (Iran): constraints from collisional and earlier deformation. Int. J. Earth Sci. 94, 401–419. https://doi.org/10.1007/s00531-005-0481-4.

Agard, P., Jolivet, L., Vrielynck, B., Burov, E., Monie, P., 2007. Plate acceleration: the obduction trigger? Earth Planet. Sci. Lett. 258, 428–441. https://doi.org/10.1016/j.epsl.2007.04.002.

Agard, P., Omrani, J., Jolivet, L., Whitechurch, H., Vrielynck, B., Spakman, W., Monié, P., Meyer, B., Wortel, R., 2011. Zagros orogeny: a subduction-dominated process. Geol. Mag. 148, 692–725. https://doi.org/10.1017/S001675681100046X.

Aid, K., Richards, P., 1980. Quantitative Seismology: Theory and Methods. Freeman, San Francisco.

Allen, M.B., Kheirkhah, M., Emami, M.H., Jones, S.J., 2011. Right-lateral shear across Iran and kinematic change in the Arabia—Eurasia collision zone. Geophys. J. Int. 184, 555–574. https://doi.org/10.1111/j.1365-246X.2010.04874.x.

Ambraseys, N.N., Melville, C.P., 2005. A History of Persian Earthquakes. Cambridge university press.

Amirihanza, H., Shafieibafti, S., Derakhshani, R., Khojastehfar, S., 2018. Controls on Cu mineralization in central part of the Kerman porphyry copper belt, SE Iran: constraints from structural and spatial pattern analysis. J. Struct. Geol. 116, 159–177. https://doi.org/10.1016/j.jsg.2018.08.010.

Angelier, J.t., Mechler, P., 1977. Sur une methode graphique de recherche des contraintes principales egalement utilisables en tectonique et en seismologie: la methode des diedres droits. Bulletin de la Société géologique de France 7, 1309–1318. https://doi.org/10.2113/gssgfbull.S7-XIX.6.1309.

Aubourg, C., Smith, B., Bakhtari, H., Guya, N., Eshragi, A., Lallemant, S., Molinaro, M., Braud, X., Delaunay, S., 2004. Post-Miocene shortening pictured by magnetic fabric across the Zagros-Makran syntaxis (Iran). Geological Society of America special paper 383, 17–40.

Aubourg, C., Smith, B., Bakhtari, H., Guya, N., Eshraghi, A., 2008. Tertiary block rotations in the Fars arc (Zagros, Iran). Geophys. J. Int. 173, 659–673. https://doi.org/10.1111/j.1365-246X.2008.03732.x.

Berberian, M., 2005. The 2003 Bam urban earthquake: a predictable seismotectonic pattern along the western margin of the rigid Lut block, southeast Iran. Earthquake Spectra 21 (S1), 35e99. https://doi.org/10.1193/1.2127909.

Bott, M.H.P., 1959. The mechanics of oblique slip faulting. Geol. Mag. 96, 109–117. https://doi.org/10.1017/S0016756800059987.

Bus, Z., Grenerczy, G., Tóth, L., Mónus, P., 2009. Active crustal deformation in two seismogenic zones of the Pannonian region—GPS versus seismological observations. Tectonophysics 474, 343–352. https://doi.org/10.1016/j.tecto.2009.02.045.

Childs, C., 2004. Interpolating surfaces in ArcGIS spatial analyst. ArcUser, July–September 3235, 569.

Dehghani, G.A., Makris, J., 1984. The gravity field and crustal structure of Iran. N. Jb. Geol. Palaeont. Abh 168, 215e229. https://doi.org/10.1127/njgpa/168/1984/215.

Delvaux, D., Sperner, B., 2003. Stress tensor inversion from fault kinematic indicators and focal mechanism data: the TENSOR program. In: New Insights Into Structural Interpretation and Modelling. vol. 212. pp. 75–100. https://doi.org/10.1144/GSL.SP.2003.212.01.06.

Delvaux, D., Moeys, R., Stapel, G., Petit, C., Levi, K., Miroshnichenko, A., Ruzhich, V., San'kov, V., 1997. Paleostress reconstructions and geodynamics of the Baikal region, Central Asia, part 2. Cenozoic rifting. Tectonophysics 282, 1–38. https://doi.org/10.1016/S0040-1951(97)00210-2.

DeMets, C., Gordon, R.G., Argus, D.F., Stein, S., 1994. Effect of recent revisions to the geomagnetic reversal time scale on estimates of current plate motions. Geophys. Res. Lett. 21, 2191–2194. https://doi.org/10.1029/94GL02118.

Derakhshani, R., Eslami, S., 2011. A new viewpoint for seismotectonic zoning. Am. J. Environ. Sci. 7, 212–218. https://doi.org/10.3844/ajessp.2011.212.218.

Derakhshani, R., Farhoudi, G., 2005. Existence of the Oman Line in the Empty Quarter of Saudi Arabia and its continuation in the Red Sea. J. Appl. Sci. 5, 745–752. https://doi.org/10.3923/jas.2005.745.752.

Fattahi, M., Walker, R., Talebian, M., Sloan, R., Rasheedi, A., 2011. The structure and late Quaternary slip rate of the Rafsanjan strike-slip fault, SE Iran. Geosphere 7, 1159–1174. https://doi.org/10.1130/GES00651.1.

Firouzkouhi, Z., Ahmadi, A., Lentz, D.R., Moridi-Farimani, A.-A., 2017. Mixing of basaltic and andesitic magmas in the Bazman volcanic field of southeastern Iran as inferred from plagioclase zoning. Mineral. Mag. 81, 975–985. https://doi.org/10.1180/minmag.2017.081.001.

Foroutan, M., Meyer, B., Sébrier, M., Nazari, H., Murray, A., Le Dortz, K., Shokri, M., Arnold, M., Aumaître, G., Bourlès, D., 2014. Late Pleistocene-Holocene right slip rate and paleoseismology of the Nayband fault, western margin of the Lut block, Iran. Journal of Geophysical Research: Solid Earth 119, 3517–3560. https://doi.org/10.1002/2013JB010746.

Ghodsi, M.R., Boomeri, M., Bagheri, S., Ishiyama, D., Corfu, F., 2016. Geochemistry, zircon U-Pb age, and tectonic constraints on the Bazman granitoid complex, southeast Iran. Turk. J. Earth Sci. 25, 311–340. https://doi.org/10.3906/yer-1509-3.

Gibbons, J.D., Chakraborti, S., 2011. Nonparametric Statistical Inference. Springer.

Gillard, D., Wyss, M., 1995. Comparison of strain and stress tensor orientation: application to Iran and southern California. Journal of Geophysical Research: Solid Earth

100, 22197–22213. https://doi.org/10.1029/95JB01871.
Gupta, T.D., Riguzzi, F., Dasgupta, S., Mukhopadhyay, B., Roy, S., Sharma, S., 2015. Kinematics and strain rates of the Eastern Himalayan Syntaxis from new GPS campaigns in Northeast India. Tectonophysics 655, 15–26. https://doi.org/10.1016/j.tecto.2015.04.017.
Hanks, T.C., Kanamori, H., 1979. A moment magnitude scale. Journal of Geophysical Research: Solid Earth 84, 2348–2350. https://doi.org/10.1029/JB084iB05p02348.
Hashemi, F., Derakhshani, R., Bafti, S.S., Raoof, A., 2018. Morphometric dataset of the alluvial fans at the southern part of Nayband fault, Iran. Data in brief 21, 1756–1763. https://doi.org/10.1016/j.dib.2018.11.017.
Jackson, J., 1992. Partitioning of strike-slip and convergent motion between Eurasia and Arabia in eastern Turkey and the Caucasus. Journal of Geophysical Research: Solid Earth 97, 12471–12479. https://doi.org/10.1029/92JB00944.
Jackson, J., McKenzie, D., 1988. The relationship between plate motions and seismic moment tensors, and the rates of active deformation in the Mediterranean and Middle East. Geophys. J. Int. 93, 45–73. https://doi.org/10.1111/j.1365-246X.1988.tb01387.x.
Kermani, A.F., Derakhshani, R., Bafti, S.S., 2017. Data on morphotectonic indices of Dashtekhak district, Iran. Data in brief 14, 782–788. https://doi.org/10.1016/j.dib.2017.08.052.
Khorrami, F., Vernant, P., Masson, F., Nilfouroushan, F., Mousavi, Z., Nankali, H., Saadat, S.A., Walpersdorf, A., Hosseini, S., Tavakoli, P., Aghamohammadi, A., Alijanzade, M., 2019. An up-to-date crustal deformation map of Iran using integrated campaign-mode and permanent GPS velocities. Geophys. J. Int. 217, 832–843. https://doi.org/10.1093/gji/ggz045.
Kostrov, V., 1974. Seismic moment and energy of earthquakes, and seismic flow of rock. Izv. Acad. Sci. USSR Phys. Solid Earth 1, 23–44. https://doi.org/10.1016/0148-9062(76)90256-4.
Lacombe, O., Mouthereau, F., Kargar, S., Meyer, B., 2006. Late Cenozoic and modern stress fields in the western Fars (Iran): implications for the tectonic and kinematic evolution of central Zagros. Tectonics 25. https://doi.org/10.1029/2005TC001831.
Lund, B., Townend, J., 2007. Calculating horizontal stress orientations with full or partial knowledge of the tectonic stress tensor. Geophys. J. Int. 170, 1328–1335. https://doi.org/10.1111/j.1365-246X.2007.03468.x.
Malvern, L.E., 1969. Introduction to the Mechanics of a Continuous Medium.
Masson, F., Chéry, J., Hatzfeld, D., Martinod, J., Vernant, P., Tavakoli, F., Ghafory-Ashtiani, M., 2005. Seismic versus aseismic deformation in Iran inferred from earthquakes and geodetic data. Geophys. J. Int. 160, 217–226. https://doi.org/10.1111/j.1365-246X.2004.02465.x.
Means, W.D., 2012. Stress and Strain: Basic Concepts of Continuum Mechanics for Geologists. Springer Science & Business Mediahttps://doi.org/10.1007/2F978-1-4613-9371-9.
Mehrabi, A., Dastanpour, M., Radfar, S., Vaziri, M., Derakhshani, R., 2015. Detection of fault lineaments of the Zagros fold-thrust belt based on Landsat imagery interpretation and their relationship with Hormuz series salt dome locations using GIS analysis. Geosciences 24, 17–32. https://doi.org/10.22071/gsj.2015.41666.
Meyer, B., Le Dortz, K., 2007. Strike-slip kinematics in central and eastern Iran: estimating fault slip-rates averaged over the Holocene. Tectonics 26. https://doi.org/10.1029/2006TC002073.
Mirzaie, A., Bafti, S.S., Derakhshani, R., 2015. Fault control on Cu mineralization in the Kerman porphyry copper belt, SE Iran: a fractal analysis. Ore Geol. Rev. 71, 237–247. https://doi.org/10.1016/j.oregeorev.2015.05.015.
National Geophysical Data Center, NOAA, 2016. National Geophysical Data Center/World Data Service (NGDC/WDS): Significant Earthquake Database. https://doi.org/10.7289/V5TD9V7K.
Navabpour, P., Angelier, J., Barrier, E., 2007. Cenozoic post-collisional brittle tectonic history and stress reorientation in the High Zagros Belt (Iran, Fars Province). Tectonophysics 432, 101–131. https://doi.org/10.1016/j.tecto.2006.12.007.
Navabpour, P., Angelier, J., Barrier, E., 2008. Stress state reconstruction of oblique collision and evolution of deformation partitioning in W-Zagros (Iran, Kermanshah). Geophys. J. Int. 175, 755–782. https://doi.org/10.1111/j.1365-246X.2008.03916.x.
Nilforoushan, F., Masson, F., Vernant, P., Vigny, C., Martinod, J., Abbassi, M., Nankali, H., Hatzfeld, D., Bayer, R., Tavakoli, F., 2003. GPS network monitors the Arabia-Eurasia collision deformation in Iran. J. Geod. 77, 411–422. https://doi.org/10.1007/s00190-003-0326-5.
Norabuena, E., Dixon, T.H., Schwartz, S., DeShon, H., Newman, A., Protti, M., Gonzalez, V., Dorman, L., Flueh, E.R., Lundgren, P., 2004. Geodetic and seismic constraints on some seismogenic zone processes in Costa Rica. Journal of Geophysical Research: Solid Earth 109. https://doi.org/10.1029/2003JB002931.
Pancha, A., Anderson, J.G., Kreemer, C., 2006. Comparison of seismic and geodetic scalar moment rates across the Basin and Range Province. Bull. Seismol. Soc. Am. 96, 11–32. https://doi.org/10.1785/0120040166.
Raeesi, M., Zarifi, Z., Nilfouroushan, F., Boroujeni, S.A., Tiampo, K., 2017. Quantitative analysis of seismicity in Iran. Pure Appl. Geophys. 174, 793–833. https://doi.org/10.1007/s00024-016-1435-4.
Rahbar, R., Shafiei Bafti, S., Derakhshani, R., 2017. Investigation of the tectonic activity of Bazargan Mountain in Iran. Sustainable Development of Mountain Territories 9, 380–386. https://doi.org/10.21177/1998-4502-2017-9-4-380-386.
Rahnamarad, J., Derakhshani, R., Farhoudi, G., Ghorbani, H., 2008. Basement Faults and Salt Plug Emplacement in the Arabian Platform in Southern Iran. J. Appl. Sci. 8, 3235–3241. https://doi.org/10.3923/jas.2008.3235.3241.
Rashidi, A., Khatib, M.M., Mosavi, S.M., Jamor, Y., 2017. Estimation of the active faults, based on Seismic, geologic and geodetic moment rates in the South and West of Lut block. J. Geosci. 26, 211–222. https://doi.org/10.22071/gsj.2017.50265.
Rashidi Boshrabadi, A., Khatib, M.M., Raeesi, M., Mousavi, S.M., Djamour, Y., 2018. Geometric-kinematic characteristics of the main faults in the W-SW of the Lut Block (SE Iran). J. Afr. Earth Sci. 139, 440–462. https://doi.org/10.1016/j.jafrearsci.2017.12.027.
Rasouli, J., Ghorbani, M., Ahadnejad, V., Poli, G., 2016. Calk-alkaline magmatism of Jebal-e-Barez plutonic complex, SE Iran: implication for subduction-related magmatic arc. Arab. J. Geosci. 9, 287. https://doi.org/10.1007/s12517-015-2124-9.
Regard, V., Bellier, O., Thomas, J.-C., Bourles, D., Bonnet, S., Abbassi, M., Braucher, R., Mercier, J., Shabanian, E., Soleymani, S., 2005. Cumulative right-lateral fault slip rate across the Zagros—Makran transfer zone: role of the Minab—Zendan fault system in accommodating Arabia—Eurasia convergence in Southeast Iran. Geophys. J. Int. 162, 177–203. https://doi.org/10.1111/j.1365-246X.2005.02558.x.
Regard, V., Bellier, O., Braucher, R., Gasse, F., Bourlès, D., Mercier, J., Thomas, J.-C., Abbassi, M., Shabanian, E., Soleymani, S., 2006. 10Be dating of alluvial deposits from Southeastern Iran (the Hormoz Strait area). Palaeogeogr. Palaeoclimatol. Palaeoecol. 242, 36–53. https://doi.org/10.1016/j.palaeo.2006.05.012.
Regard, V., Hatzfeld, D., Molinaro, M., Aubourg, C., Bayer, R., Bellier, O., Yamini-Fard, F., Peyret, M., Abbassi, M., 2010. The transition between Makran subduction and the Zagros collision: recent advances in its structure and active deformation. Geol. Soc. Lond., Spec. Publ. 330, 43–64. https://doi.org/10.1144/SP330.4.
Şengör, A.M.C., Altlner, D., Cin, A., Ustaomer, T., Hsu, K.J., 1988. Origin and assembly of the Tethyside orogenic collage at the expense of Gondwana land. In: AudleyCharles, M.G., Hallam, A.E. (Eds.), Gondwana and Tethys. Geological Society of London Special Publication. Blackwell, Oxford, pp. 119e181. https://doi.org/10.1144/GSL.SP.1988.037.01.09.
Vernant, P., Nilforoushan, F., Hatzfeld, D., Abbassi, M., Vigny, C., Masson, F., Nankali, H., Martinod, J., Ashtiani, A., Bayer, R., 2004. Present-day crustal deformation and plate kinematics in the Middle East constrained by GPS measurements in Iran and northern Oman. Geophys. J. Int. 157, 381–398. https://doi.org/10.1111/j.1365-246X.2004.02222.x.
Walker, R., Talebian, M., Sloan, R., Rasheedi, A., Fattahi, M., Bryant, C., 2010. Holocene slip-rate on the Gowk strike-slip fault and implications for the distribution of tectonic strain in eastern Iran. Geophys. J. Int. 181, 221–228. https://doi.org/10.1111/j.1365-246X.2010.04538.x.
Walpersdorf, A., Manighetti, I., Mousavi, Z., Tavakoli, F., Vergnolle, M., Jadidi, A., Hatzfeld, D., Aghamohammadi, A., Bigot, A., Djamour, Y., 2014. Present-day kinematics and fault slip rates in eastern Iran, derived from 11 years of GPS data. Journal of Geophysical Research: Solid Earth 119, 1359–1383. https://doi.org/10.1002/2013JB010620.
Ward, S.N., 1998. On the consistency of earthquake moment rates, geological fault data, and space geodetic strain: the United States. Geophys. J. Int. 134, 172–186. https://doi.org/10.1046/j.1365-246x.1998.00556.x.
Wesnousky, S.G., 1988. Seismological and structural evolution of strike-slip faults. Nature 335 (6188), 340e343. https://doi.org/10.1038/335340a0.
Zamani, B., Angelier, J., Zamani, A., 2008. State of stress induced by plate convergence and stress partitioning in northeastern Iran, as indicated by focal mechanisms of earthquakes. J. Geodyn. 45, 120–132. https://doi.org/10.1016/j.jog.2007.07.003.
Zanchi, A., Berra, F., Mattei, M., Ghassemi, M.R., Sabouri, J., 2006. Inversion tectonics in central Alborz, Iran. J. Struct. Geol. 28, 2023–2037. https://doi.org/10.1016/j.jsg.2006.06.020.
Zarifi, Z., Nilfouroushan, F., Raeesi, M., 2014. Crustal stress map of Iran: insight from seismic and geodetic computations. Pure Appl. Geophys. 171, 1219–1236. https://doi.org/10.1007/s00024-013-0711-9.
Zoback, M.L., 1992a. First-and second-order patterns of stress in the lithosphere: the World Stress Map Project. Journal of Geophysical Research: Solid Earth 97, 11703–11728. https://doi.org/10.1029/92JB00132.
Zoback, M.L., 1992b. Stress field constraints on intraplate seismicity in eastern North America. Journal of Geophysical Research: Solid Earth 97, 11761–11782. https://doi.org/10.1029/92JB00221.